

Diagnosing the interstellar medium of galaxies with far-infrared emission lines

II. [C II], [O I], [O III], [N II] and [N III] up to $z=6$

Andrés F. Ramos Padilla^{*1,2}, L. Wang^{1,2}, F. F. S. van der Tak^{1,2}, and S. C. Trager¹

¹ Kapteyn Astronomical Institute, University of Groningen, Landleven 12, 9747 AD, Groningen, the Netherlands

² SRON Netherlands Institute for Space Research, Landleven 12, 9747 AD, Groningen, the Netherlands

Received September 15, 1996; accepted March 16, 1997

ABSTRACT

Context. Gas cooling processes in the interstellar medium (ISM) are key to understanding how star-formation processes occur in galaxies. Far-infrared (FIR) fine-structure emission lines can be used as a tool to understand the gas conditions and trace the different phases of the ISM.

Aims. We model the most important far-infrared (FIR) emission lines throughout cosmic time back to $z = 6$ with cosmological hydrodynamical simulations. We study how different physical parameters, such as the interstellar radiation field (ISRF) and metallicity, impact the ISM phases traced by FIR line luminosities and connect those with the star-formation rate (SFR).

Methods. We implement a physically motivated multi-phase model of the ISM by post-processing EAGLE cosmological simulation with CLOUDY look-up tables. In this model, we assume four phases of the ISM: dense molecular gas, neutral atomic gas, diffuse ionised gas (DIG) and HII regions.

Results. Our model shows good agreement with the observed luminosity–SFR relation up to $z = 6$ in the FIR emission lines analysed and we also provide linear fits. Our predictions also agree with observations in terms of diagnostic diagrams involving various line ratios.

Conclusions. We find that [C II] is the best SFR tracer of the FIR lines even though it traces multiple ISM phases, while [O III] and [N II] can be used to understand the DIG-HII balance in the ionised phase. In addition, line ratios like [C II]/[O III] and [N II]/[O I] are useful to trace parameters such as ISRF, metallicity and specific star-formation rate. These results help to interpret observations of FIR line emission from the local Universe to high- z galaxies.

Key words. Galaxies: ISM, star formation, high-redshift – ISM: lines and bands, structure – Infrared: ISM – methods: numerical

1. Introduction

After the Universe was largely ionised (the period known as “cosmic dawn” at $z \lesssim 6-8$), the composition of the gas and its cooling gradually changed, affecting the star-formation processes in galaxies (Dayal & Ferrara 2018). Since then, star formation and black hole accretion processes co-evolved with cosmic time and shaped the evolution of galaxies (Madau & Dickinson 2014). The study of the interstellar medium (ISM) in the local Universe allows us to comprehend the current star-formation processes, but the ISM gas cooling budget may not be the same at earlier cosmic epochs (Carilli & Walter 2013). Recent observational data have opened new paths for describing and understanding the ISM gas processes of local galaxies (e.g. Malhotra et al. 2001; De Looze et al. 2014; Cormier et al. 2015). However, the complete picture of how the ISM evolves over cosmic time and how its conditions are connected with star formation in galaxies is not well understood.

Far-infrared (FIR) fine-structure emission lines (Table 1) are dominant in the gas cooling of the ISM and can help us to understand the star-formation processes, from a theoretical (e.g. Tielens & Hollenbach 1985; Goldsmith et al. 2012; Wolfire et al.

2022) and observational perspective (e.g. Ferkinhoff et al. 2010; Carilli & Walter 2013; Cormier et al. 2015; Díaz-Santos et al. 2017; Herrera-Camus et al. 2018b). These lines are less affected by dust extinction than optical lines and, at high redshift (hereafter high- z), are shifted to the (sub-)mm wavelength range accessible to ground-based telescopes (Hodge & da Cunha 2020; Förster Schreiber & Wuyts 2020). The most important ISM emission cooling line is [C II] at $158 \mu\text{m}$. This line traces different phases of the ISM: photo-dissociation regions (PDRs), HII regions, diffuse ionised gas (DIG; also known as the warm ionised medium (WIM), e.g. Haffner et al. 2009; Kewley et al. 2019), molecular clouds, and the cold and warm neutral media (CNM and WNM, respectively) (e.g. Cormier et al. 2012; Croxall et al. 2017; Abdullah et al. 2017; Abdullah & Tielens 2020). [C II] is thus a very important cooling line in the range of 20–8000 K due to its low ionisation potential (11.3 eV compared to 13.6 eV for hydrogen: Gong et al. 2012; Goldsmith et al. 2012). Furthermore, it is easily observable, as its luminosity is around 1% of the FIR luminosity of galaxies (e.g. Stacey et al. 1991; Brauher et al. 2008). Other important FIR lines include: i) atomic oxygen ([O I]) at 63 and $145 \mu\text{m}$, which traces the denser and warmer neutral ISM environments important for star formation (Malhotra et al. 2001; Goldsmith 2019); ii) ionised nitrogen ([N II] at

* e-mail: ramos@astro.rug.nl

Table 1. Important FIR fine-structure emission lines. Data from Kramida et al. (2020) and Spinoglio et al. (2017).

Line Species	λ [μm]	Transition	IP [eV]	n_{crit} [cm^{-3}]
[O III]	51.81	$^3\text{P}_2 - ^3\text{P}_1$	35.12	3.6×10^3
[N III]	57.34	$^2\text{P}_{3/2} - ^2\text{P}_{1/2}$	29.60	3.0×10^3
[O I]	63.18	$^3\text{P}_2 - ^3\text{P}_1$...	4.7×10^5
[O III]	88.36	$^3\text{P}_1 - ^3\text{P}_0$	35.12	5.1×10^2
[N II]	121.80	$^3\text{P}_1 - ^3\text{P}_0$	14.53	3.1×10^2
[O I]	145.53	$^3\text{P}_1 - ^3\text{P}_0$...	9.5×10^4
[C II]	157.68	$^2\text{P}_{3/2} - ^2\text{P}_{1/2}$	11.26	2.8×10^3
[N II]	205.30	$^3\text{P}_2 - ^3\text{P}_1$	14.53	4.8×10^1

122 and 205 μm , which traces the ionised medium from DIG and HII regions (in the local Universe, Cormier et al. 2012; Goldsmith et al. 2015; Zhao et al. 2016a; Croxall et al. 2017; Langer et al. 2021, and at high- z , e.g. Pavesi et al. 2016); iii) [O III] at 52 and 88 μm , which traces HII regions around young stars (at high- z Ferkinhoff et al. 2010; Inoue et al. 2014); and iv) [N III] at 57 μm , which also traces HII regions (Nagao et al. 2011). Using these lines to understand the ISM evolution of galaxies requires a self-consistent model for all of these FIR lines over the $z = 0-6$ range.

For many decades, the lack of suitable instruments has hampered observations of these FIR lines in high- z galaxies (Inoue et al. 2014). Fortunately, observations taken with telescopes such as IRAM, CSO, *Herschel* and ALMA have provided the first high- z detections of lines like [C II], [N II], [O I] and [O III] (e.g. Maiolino et al. 2005; Ferkinhoff et al. 2010, 2011; Inoue et al. 2016; Uzgil et al. 2016). Moreover, recent emission line surveys like ALPINE (Le Fèvre et al. 2020) and REBELS (Bouwens et al. 2021) are gathering data for larger samples of high- z galaxies, which are ideal to diagnose the ISM of galaxies over cosmic time.

With these new observations, different tools can be used to describe the different physical conditions in the ISM of high- z galaxies. The most common and accessible tool is the use of emission line ratios that reflect the physical conditions of the ISM. For example, the [C II]/[N II] ratio has been used to describe and constrain whether HII regions and/or PDRs contribute to the ISM phases of galaxies (Decarli et al. 2014), and can be used to estimate the amount of ionised gas in [C II] (Croxall et al. 2017). Another useful line ratio is [O III]/[C II], used to understand ionised and neutral gas in high- z galaxies (e.g. Harikane et al. 2020; Carniani et al. 2020). This ratio has the advantage that [O III] can be brighter than [C II] at redshifts around the reionisation epoch ($z \gtrsim 7$, Inoue et al. 2014, 2016) and can be observed efficiently with ALMA (Bouwens et al. 2021). Finally, the [O III]/[N III] ratio is used to estimate the gas metallicities (Nagao et al. 2011; Herrera-Camus et al. 2018a), although other line ratios can also be used for this purpose (Fernández-Ontiveros et al. 2021).

A more sophisticated tool to describe the physical processes of the ISM is the use of line luminosity predictions from simulations or analytical models. Simple models involve ratios between FIR emission lines and/or the total luminosity in the IR to obtain physical conditions such as hydrogen density, FUV radiation flux or stellar temperatures (e.g. Malhotra et al. 2001; Ferkinhoff et al. 2011), while more complex models use magneto-radiation hydrodynamics simulations of the Universe with different radiative transfer codes to predict emission line luminosities

(e.g. Olsen et al. 2021; Katz et al. 2022; Pallottini et al. 2022, and references therein). Some of these studies focus on specific emission lines such as [C II], [O I] or [O III] in analytic models (e.g. Goldsmith 2019; Ferrara et al. 2019; Yang & Lidz 2020) and simulations (e.g. Moriwaki et al. 2018; Leung et al. 2020; Ramos Padilla et al. 2021), while others study interesting line ratios like [O III]/[C II] (Arata et al. 2020; Vallini et al. 2021). A large effort has also been made to model various FIR emission lines in models at different cosmic times (e.g. Vallini et al. 2013, 2015; Olsen et al. 2015, 2017, 2021; Popping et al. 2019; Sun et al. 2019; Katz et al. 2019, 2022; Pallottini et al. 2019; Yang et al. 2021b, 2022). However, these studies do not examine the emission of these FIR lines in a consistent way in terms of their redshift evolution, from the local Universe to the epoch of reionisation, due to computational constraints or focus on certain cosmic epochs (with the exception of Popping et al. (2019) which modelled the [C II] line). Therefore, we need better models to understand current observations consistently.

With this in mind, we aim to predict luminosities of the main FIR lines in a cosmological context through the use of cosmological hydrodynamical simulations to infer the physical conditions of galaxies across a wide range of redshifts. The goal of this paper is to test the impact of physical parameters on the FIR emission lines tracing different ISM phases in galaxies. We will use these predictions as diagnostic tools, which will be useful for both current and future observations. To do this, we model the emission of FIR lines by post-processing the hydrodynamical simulations of the Evolution and Assembly of Galaxies and their Environments (EAGLE) project (Schaye et al. 2015; Crain et al. 2015) with a physically motivated model of the ISM presented in Ramos Padilla et al. (2021, hereafter Paper I). We use CLOUDY (Ferland et al. 2017) cooling tables (Ploeckinger & Schaye 2020) to predict the emission from different ISM phases in galactic environments. Throughout this paper, we assume the Λ CDM cosmology from the Planck Collaboration et al. (2014) results ($\Omega = 0.307$, $\Omega_\Lambda = 0.693$, $H_0 = 67.7 \text{ km s}^{-1} \text{ Mpc}^{-1}$ and $\sigma_8 = 0.8288$).

In this paper, we first briefly describe the simulation data and the ISM model that we use to predict FIR emission line luminosities (Sect. 2). Next, we present the results of the FIR emission line predictions from the simulations and how they compare with the observations from the local Universe all the way out to $z \sim 6$ (Sect. 3). In Sect. 4 we evaluate some FIR diagnostic diagrams used in various high- z studies. After that, we discuss the potential systematic uncertainties that can affect the predictions and the comparisons with observations (Sect. 5). Finally, we present our conclusions in Sect. 6.

2. Methodology

In this section, we first describe the sets of simulations that we use in this work (Sect. 2.1), then we briefly explain the initial model used to characterise the structure of the ISM (Sect. 2.2). Finally, we present in detail the addition of HII regions as a new ISM phase (Sect. 2.3) in our model.

2.1. The EAGLE simulations

EAGLE (Schaye et al. 2015; Crain et al. 2015) is a suite of cosmological hydrodynamical simulations which were run using a modified version of GADGET-3 (last described by Springel 2005), a smoothed-particle hydrodynamics (SPH) code. Briefly, EAGLE adopts an SPH pressure-entropy parameterisation following Hopkins (2013). The simulations include radiative cool-

ing and photo-electric heating (Wiersma et al. 2009a), star formation (Schaye & Dalla Vecchia 2008), stellar evolution and mass loss (Wiersma et al. 2009b), black hole growth (Springel et al. 2005; Rosas-Guevara et al. 2015), and feedback from star formation and active galactic nuclei (AGN) (Dalla Vecchia & Schaye 2012). The simulations provide the properties for gas, dark matter, stellar and supermassive black hole SPH particles.

For this work, based on the results from Paper I, we used two simulations from the EAGLE suite: REF-L0100N1504 and RECAL-L0025N0752, as described in Table 2. The main differences between the two simulations are the box-size of the simulation (100 and 25 cMpc (comoving Mpc), respectively), the mass resolution ($\sim 10^6 M_\odot$ and $\sim 10^5 M_\odot$, respectively), and the calibration of the physical parameters of the subgrid routines to reproduce the galaxy stellar mass function (GSMF; Schaye et al. 2015). Both simulations are similar in terms of “weak convergence”, which means numerical results converge in different simulations after re-calibrating the sub-grid parameters (Furlong et al. 2015; Schaye et al. 2015).

In this study, we retrieve simulated galaxies from the SPH data (The EAGLE team 2017) by using textscFoF (Friends-of-Friends) and SUBFIND algorithms (Springel et al. 2001; Dolag et al. 2009) in the dark matter halos. With these algorithms, the sub-halos containing the particle with the lowest value of the gravitational potential are called “central” galaxies. We focus on these “central” galaxies to estimate line luminosities. We use galaxies with at least 300 star particles (i.e. stellar masses higher than $\sim 10^8 M_\odot$ and $\sim 10^{8.5} M_\odot$ for RECAL-L0025N0752 and REF-L0100N1504, respectively) within 30 kpc (proper kpc) from the centre of the potential. We selected our sample of galaxies from the EAGLE database (McAlpine et al. 2016) in redshifts (the closest snapshot) between $z = 0$ and $z = 6$ in steps of $\Delta z = 1$, using a single snapshot at each redshift (the snapshot closest in time; e.g. at $z = 6$, we use the $z = 5.97$ snapshot from EAGLE), where the total number of galaxies depends on the simulation used. The $z = 6$ cutoff was selected due to the availability of observational data and the number of galaxies recovered in EAGLE required to compare them statistically. For RECAL-L0025N0752, we select all retrieved galaxies, while for REF-L0100N1504, we randomly select up to 1 000 galaxies that fulfil the previous conditions per redshift. In the last columns of Table 2, we present the total number of galaxies used per redshift slice in each of the simulations.

We selected a total sample of 8 277 galaxies simulated with EAGLE at redshifts between $z = 0$ and $z = 6$. In each of those galaxies, we model the emission coming from the eight FIR emission lines (Table 1) that trace different phases of the ISM.

2.2. The multi-phase ISM model

To predict these emission lines, we used the ISM model presented in Paper I, where the luminosity estimations from the [C II] emission line at $158 \mu\text{m}$ in the local Universe ($z = 0$) showed good agreement with observations. However, this model must be improved if we want to properly account for other FIR lines such as [O III] and [N III], which probe denser ionised regimes. Therefore, we add H II regions as a new phase in our ISM model. In Fig. 1, we illustrate the path from the EAGLE simulations (Sect. 2.1) to the total luminosity of the lines in the current model. The main difference between Paper I and this work is the addition of the contribution to the line luminosities from H II regions (Sect. 2.3). In this subsection, we briefly explain the model presented in Paper I.

After selecting the sample of galaxies for which we want to calculate the line luminosity, we retrieve and post-process the gas and star particle data of the galaxies in the simulation. Physical properties such as total hydrogen number density were estimated for all gas particles using the information available in the SPH particle data. For example, we calculated the total hydrogen number density as $n(\text{H}) = \frac{\rho X_{\text{H}}}{m_{\text{H}}}$, with m_{H} the hydrogen mass, ρ the density and X_{H} the SPH weighted hydrogen abundance. In addition, the fraction of neutral hydrogen was estimated for all gas particles according to Rahmati et al. (2013), following ionisation equilibrium as described in Sect. 2.2.1 in Paper I. We calculated the background interstellar radiation field (ISRF) from the star formation rate (SFR) surface density of the gas particles and the local ISRF from the star particles as described by Olsen et al. (2017). The local ISRF is estimated with starburst99 models (Leitherer et al. 2014) for star particles with a distance below the smoothing length of a given gas particle (as described in Sect. 2.2.1 in Paper I). The sum of the background ISRF and the local ISRF defines the total ISRF impinging on the neutral cloud. With the fraction of neutral hydrogen, we split the gas into neutral and ionised components. The neutral gas mass and the ISRF are used to estimate the sizes of the neutral clouds, while the ionised mass is used to describe the diffuse ionised gas (DIG).

The neutral clouds are defined as concentric spheres with densities following a Plummer profile. Each ISM phase in the neutral cloud is defined by a different radius as described in Sect. 2. in Paper I. The transition between atomic and molecular hydrogen defines the limit between the neutral atomic gas and the dense molecular gas, while the transition between ionised to neutral carbon defines the limit for the inner core region of the cloud that is completely shielded from FUV radiation. This definition assumes that the inner core can only be traced by neutral species such as CO, and the inner core is therefore ignored in the estimation of the total luminosity of the FIR emission lines¹.

On the other hand, the volumetric structure of the DIG is assumed to be spherical with a radius drawn from a smoothed broken power-law distribution. The parameters of the power-law distribution are derived based on calibrating the [N II] line (at 122 and $205 \mu\text{m}$) predictions of 492 galaxies from the REF-L0100N1504 and 200 galaxies from RECAL-L0025N0752 simulations to the observational dataset from Spinoglio et al. (2015), Fernández-Ontiveros et al. (2016) and Cormier et al. (2019) (containing 8, 53 and 2 galaxies, respectively, of a sample of 63 galaxies). This led us to DIG clouds with average sizes of ~ 900 pc for RECAL-L0025N0752 galaxies and ~ 2 kpc for REF-L0100N1504, which is around 3 times the maximum softening length of the original simulations.

These structures define the phases of the ISM that contribute to the total luminosity of the emission line: DIG, neutral atomic and dense molecular gas. The estimation of the luminosities for each phase is obtained by using CLOUDY (v17.01, Ferland et al. 2017) cooling tables of shielded and optically thin gas (Ploeckinger & Schaye 2020). The sum of those phases then gives us the total luminosity for a FIR emission line. For a complete description of the model, we refer the reader to Sect. 2.2 and 2.3 in Paper I.

¹ [O I] emission can come also from the inner core. However, as our results show, the contribution of this inner core to the [O I] luminosity is usually very small.

Table 2. EAGLE simulations used in this work. The box-size, number of particles and gas particle mass define the resolution of the simulation. The right columns show the number of galaxies used in this work for a given simulation at each redshift.

Name in Schaye et al. (2015)	Box-size (cMpc)	Number of particles	SPH Gas mass (M_{\odot})	Number of galaxies						
				$z = 0$	$z = 1$	$z = 2$	$z = 3$	$z = 4$	$z = 5$	$z = 6$
RECAL-L0025N0752	25	752^3	2.26×10^5	415	426	339	252	154	75	37
REF-L0100N1504	100	1504^3	1.81×10^6	1000	1000	1000	1000	1000	1000	579

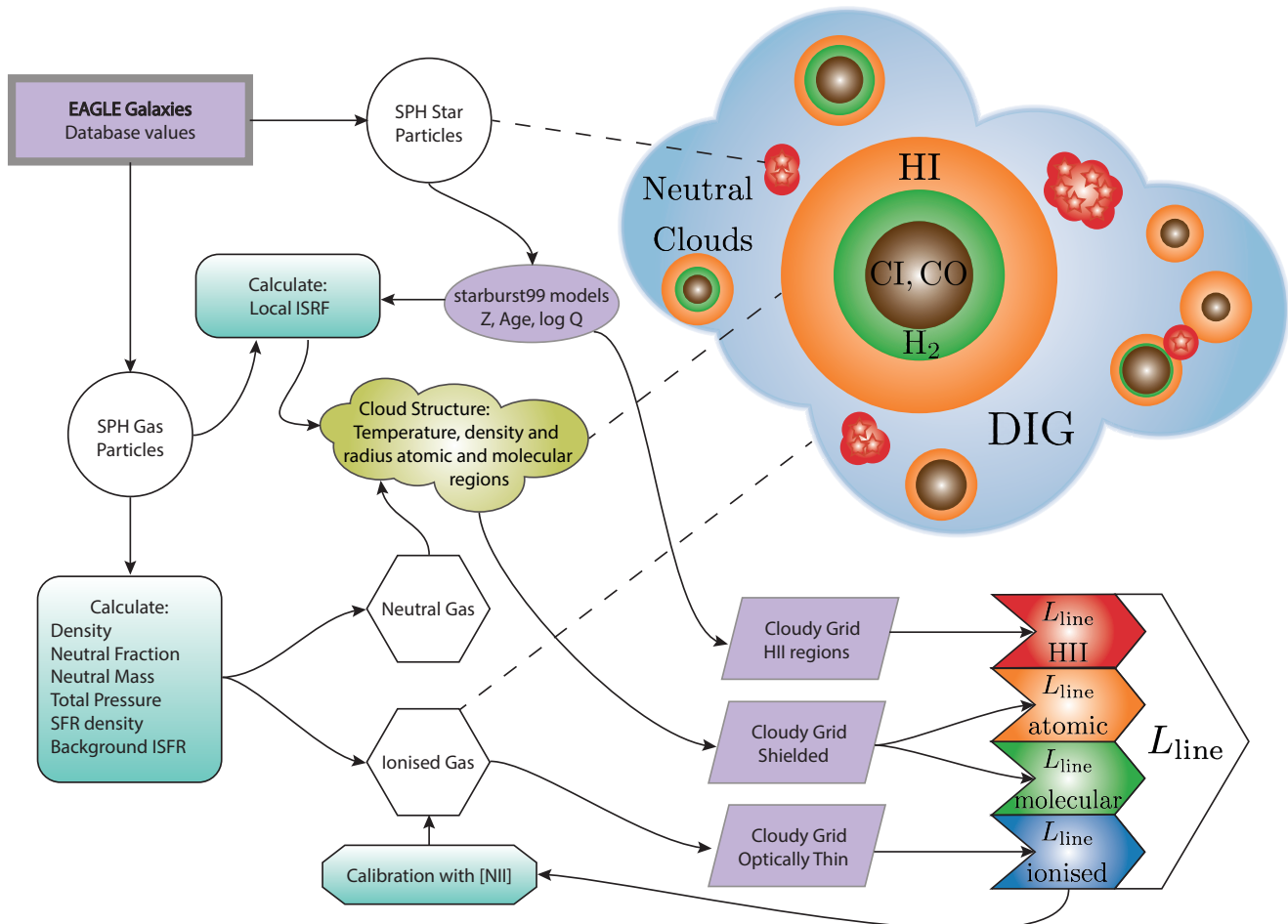


Fig. 1. Flowchart of the sub-grid procedures applied to the SPH to simulate FIR line emission in post-processing. This flowchart is similar to the one presented in [Paper I](#) with the main difference being the added HII regions as a new ISM phase. The dashed lines connect the gas and star environments to the ingredients of the model.

2.3. HII regions as a new ISM phase

The luminosity estimations for FIR lines such as [O III] and [N III], which require high ionisation potentials (35.1 and 29.6 eV, respectively), can only be found in HII regions and other dense, ionised regimes. The addition of this phase as an ISM component to the model allows us to compare the predicted luminosities of these lines with observations. Therefore, we update the model described in [Paper I](#) to simulate the HII regions production of the most prominent FIR lines, including [C II], [O III], [O I], as shown in [Table 1](#), in order to infer the ISM conditions in galaxies from the local Universe out to $z \approx 6$.

In [Paper I](#), we use `starburst99` to calculate the ISRF from the stars close to gas particles (the distance between the particles is less than one smoothing length). Now, we also use the spectrum from `starburst99` to calculate the emission coming from HII regions. To generate this spectrum, we adopted the Geneva

stellar models ([Schaller et al. 1992](#)) with standard mass loss for five metallicities ($Z = 0.001, 0.004, 0.008, 0.020, \text{ and } 0.040$). We split `starburst99` grid values in young ($\leq 100\text{Myr}$) and old ages ($> 100\text{Myr}$), to improve our estimations at younger ages. For young ages, we estimate the parameters every 1 Myr, while for old ages we calculate 100 steps on a logarithmic scale up to 10 Gyr. We assume a total stellar mass of $10^4 M_{\odot}$, with a Kroupa initial mass function (IMF). The SPH star particles are divided to match the stellar mass from the `starburst99` models, assuming a random exponential distribution of the original ages of the SPH particles. By doing this we try to avoid the poor sampling of star formation that can affect luminosity estimates, especially in HII regions.

We use a photoionisation model from `CLOUDY` to simulate the line emissivities of HII regions based on `starburst99` spectra of their underlying stellar populations. We calculate the stellar atmospheres, or spectral energy distributions (SEDs), in the

Table 3. Sampling of the properties of HII regions in the CLOUDY grid used in this work. The resulting number of grid points is 3600 per redshift.

Parameter	Unit	Min.	Max.	Interval
Metallicity	[Z _⊙]	0.075	2.991	0.324
log(<i>Q</i>)	[s ⁻¹]	52	44	1
log(Age)	[Gyr]	-3.0	0.9	0.1

photoionisation models for a given age, metallicity and the ionising photon flux (*Q*). In this way, the stellar mass and metallicity from the star SPH particles are used to obtain *Q* coming from a stellar cluster from the starburst99 grids. Thus, we use these three physical parameters (age, metallicity and *Q*) to construct spherical clouds where the emissivities depend only on them. The range of values for these parameters is presented in Table 3, totalling 25 200 grid points for all redshifts in this work.

In terms of the structure, we assume a fixed density of $\sim 30 \text{ cm}^{-3}$ to resemble classical HII regions similar to the Ström-gren sphere, where densities are in the range of $10\text{--}100 \text{ cm}^{-3}$ (Draine 2011). Choosing a higher or lower density affects the HII luminosity of some lines as we describe in Sect. 5. In ionisation balance the Ström-gren radius is

$$R_{\text{Str}} = \left(\frac{3Q}{4\pi n(\text{H})^2 \alpha_B} \right)^{1/3}, \quad (1)$$

with *Q* the ionising photon flux in units of s⁻¹, *n*(H) the total hydrogen number density in units of cm⁻³ and α_B is the Case B recombination rate coefficient.

These HII regions are radiation bound in terms of ionised hydrogen. Once the ratio of ionised hydrogen to the total hydrogen density drops below 5%, the calculation stops, which defines the outer radius. The inner radius is set to 1% of the expected Ström-gren sphere radius (Eq. 1), as in Yang & Lidz (2020), allowing us to obtain “ultracompact” HII regions, which can have sizes of $\sim 0.03 \text{ pc}$ (Kurtz 2005). We calculate the emissivities without further iteration on the assumed density, which is adequate for clouds with densities typical of HII regions (Ferland 1996). For the rest of the parameters in CLOUDY we choose a similar configuration as the one used by Ploeckinger & Schaye (2020).

The starburst99 outputs are also used to calculate the L_{FUV} and *Q* for each star SPH particle. Thus, the look-up luminosity tables from CLOUDY are used to interpolate the star SPH particles in terms of age, metallicity and *Q*. As a result, we obtain the respective HII luminosity for each star particle for the FIR emission lines. This luminosity is then used as part of the total contribution of the ISM phases (DIG + neutral atomic gas + dense molecular gas + HII regions) for a given simulated galaxy.

3. Individual line luminosities

In this section, we present the predictions of individual lines from our model and compare them with observations. For each line, we first examine the relation between the line luminosity and the SFR of the galaxy at different cosmic epochs. Our predictions of the line luminosity–SFR relation are also compared with observational measurements collected and homogenised from published work (see Appendix A). Then we check the contribution to the line luminosities from each of the ISM phases, i.e., the DIG, HII regions, neutral atomic and dense molecular gas. We mainly discuss the results of the five FIR emission lines: [C II] at $158 \mu\text{m}$, [O I] at $63 \mu\text{m}$, [N II] at $205 \mu\text{m}$, [O III] at $88 \mu\text{m}$,

and [N III] at $57 \mu\text{m}$. The other three emission lines listed in Table 1 behave similarly to their aforementioned pairs (e.g. [O III] at $52 \mu\text{m}$ is similar to [O III] at $88 \mu\text{m}$). We release all the data in a Zenodo repository as described in Appendix B.

3.1. [C II] $158 \mu\text{m}$

3.1.1. The SFR– $L_{[\text{C II}]}$ relationship

The most important and brightest of these FIR lines is [C II] at $158 \mu\text{m}$. This line follows a clear trend with SFR (e.g. Stacey et al. 1991; Braucher et al. 2008; Stacey et al. 2010), and it is used as a SFR tracer at different redshifts (e.g. De Looze et al. 2014; Herrera-Camus et al. 2015; Schaerer et al. 2020). In Fig. 2, we show the relationships between SFR and [C II] luminosity ($L_{[\text{C II}]}$) for the seven redshift slices analysed in this work. We compare the predictions from the EAGLE simulations REF-L100N1504 and RECAL-L0025N0752 with predictions from other simulations (Olsen et al. 2015, 2018; Katz et al. 2022), semi-analytic models (Lagache et al. 2018; Popping et al. 2019) and linear relationships derived from observations (De Looze et al. 2014; Schaerer et al. 2020). We also plot the linear relationships that we infer from our model (see Appendix C) and extrapolate them outside the dynamic range covered by the simulations but within $10^{-3.5} \text{ M}_{\odot} \text{ yr}^{-1} < \text{SFR} < 10^{3.5} \text{ M}_{\odot} \text{ yr}^{-1}$. With this extrapolation, we can compare the observations with high SFR values that the simulations do not cover. This is necessary as high-*z* observations generally only include galaxies with very high SFR due to sensitivity limits. In general, the agreement between our models, observations and other models is good within the typical scatter $\sim 0.4 \text{ dex}$ (De Looze et al. 2014), especially at $z = 0$ and $z = 6$, where there are more observational constraints.

In Ramos Padilla et al. (2021) we showed that the SFR– $L_{[\text{C II}]}$ relationship at $z = 0$ could be reproduced with a model similar to that implemented in this work. Therefore, it is not surprising that the current model still reproduces this SFR– $L_{[\text{C II}]}$ relationship. Compared to Popping et al. (2019), the only other model that covers the same redshift range as this work for [C II], we find a flatter slope in the SFR– $L_{[\text{C II}]}$ relationship. Especially at $z = 1\text{--}3$, the differences in the slopes can lead to up to $\sim 1.8 \text{ dex}$ change in $L_{[\text{C II}]}$ at SFRs around $1000 \text{ M}_{\odot} \text{ yr}^{-1}$, but the relationships are more similar at other redshifts. The reason for these discrepancies may reside in the different galaxy formation physics in EAGLE and the Santa Cruz SAM used in Popping et al. (2019). Unfortunately, the comparison between the two galaxy formation models is out of the scope of this work.

At $z = 2$, the linear relationship of Olsen et al. (2015) predicted from seven simulated galaxies shows a behaviour similar to that of Popping et al. (2019) and agrees with the estimated scatter of our linear regression (0.2 dex) at SFRs around $1 \text{ M}_{\odot} \text{ yr}^{-1}$. Over the redshift range $z = 1\text{--}3$, the extrapolation of our relation show a potential small offset compared with observations. However, this discrepancy is not significant, taking into account the small sample size, large scatter (around 0.5 dex), potential bias towards galaxies with high line luminosities, and systematics in deriving luminosities and SFR. Furthermore, altering the assumptions in our modelling process could affect our predictions, as we show in Sect. 5.

At $z = 4\text{--}6$, most of the models and observations match well with the linear relationships derived from our predictions. Similar predictions from Vallini et al. (2015), Leung et al. (2020) and Carniani et al. (2020), which are not shown in the plot, also agree at $z = 6$, indicating that the SFR– $L_{[\text{C II}]}$ relationship can be tight at higher redshift, even if there is some scatter in the data related

to observational errors (Schaerer et al. 2020). This demonstrates that our physically motivated model of the ISM is valid not only for estimating the luminosity of [C II] in the local Universe but also up to $z = 6$.

3.1.2. [C II] deficit

Although a linear SFR– $L_{[\text{C II}]}$ relation is commonly used to assume that $L_{[\text{C II}]}$ is a good SFR tracer, observational data of local galaxies show a decrease of $L_{[\text{C II}]}$ at IR luminosities above $10^{12} L_{\odot}$, known as the “[C II] deficit” (e.g. Díaz-Santos et al. 2017; Herrera-Camus et al. 2018b). However, recent observations of $z > 4$ galaxies show no evidence of such a deficit (Matthee et al. 2019; Carniani et al. 2020; Schaerer et al. 2020, e.g.). In Ramos Padilla et al. (2021), we examined this deficit by comparing the SFR– $L_{[\text{C II}]}$ relationship with deviations from the star-forming main-sequence (MS), following the suggestion of Herrera-Camus et al. (2018b). In this work, we compare the $L_{[\text{C II}]}/\text{SFR}$ ratio with the offset from the MS (ΔMS) in Fig. 3. We estimate the specific SFR (sSFR = SFR/ M_{\star}) of our galaxies and normalise this by the derived sSFR for the MS from Speagle et al. (2014), which gives us the ΔMS .

We find that the $L_{[\text{C II}]}/\text{SFR}$ ratio almost always decreases with ΔMS . If the decrease in the $L_{[\text{C II}]}/\text{SFR}$ ratio extends to a higher ΔMS , it supports the idea that starburst galaxies may not follow the SFR– $L_{[\text{C II}]}$ relationship shown in Fig. 2 (Herrera-Camus et al. 2018b; Ferrara et al. 2019). Therefore, $L_{[\text{C II}]}$ may not be a good tracer of SFR for starburst galaxies, as we discuss in Sect. 3.6.

3.1.3. Contribution to $L_{[\text{C II}]}$ from each ISM phase

We present the average contribution of the ISM phases to $L_{[\text{C II}]}$ at each redshift as a function of SFR for the galaxies in the RECAL-L0025N0752 simulation in Fig. 4. We examine the ISM phase contributions of the RECAL-L0025N0752 simulation because we expect this simulation to behave more like observed local galaxies, as shown in Paper I. In general, we find that most of the [C II] emission comes mainly from the atomic phase, especially at $z > 2$, in agreement with the general assumption that the neutral gas is the dominant ISM phase contributing to $L_{[\text{C II}]}$ as estimated from observations (e.g. Croxall et al. 2017; Cormier et al. 2019) and suggested by models (e.g. Olsen et al. 2015, 2018; Lagache et al. 2018). However, the contribution by neutral atomic gas to $L_{[\text{C II}]}$ changes with redshift, from $\sim 20\text{--}40\%$ at $z \leq 1$, to $\sim 70\text{--}90\%$ at $z \geq 3$. The most important reason for these differences is the contribution from the DIG. At $z = 0$, the DIG dominates (the contribution is greater than 50%) in most of the galaxies with a SFR $< 0.1 M_{\odot} \text{ yr}^{-1}$, then the DIG contribution reduces to 30% at $z = 2$, and finally it is negligible at $z = 6$. This negligible contribution of the DIG at $z = 6$ does not agree with the estimated contribution of 44% by Olsen et al. (2018). This result is expected as we estimate the size of the DIG using a physical assumption instead of using the smoothing length as in Olsen et al. (2018), which leads to a more compact DIG. However, as our modelled SFR– $L_{[\text{C II}]}$ relation shows a better agreement with observations, this may imply that a higher contribution from the atomic gas is needed to match the observed galaxies at $z = 6$. Therefore, our estimations seem to favour the atomic gas as the main responsible for the $L_{[\text{C II}]}$ at $z = 6$.

On the other hand, the fractional contribution of H II regions to $L_{[\text{C II}]}$ reaches its maximum at $z = 2$, where they contribute up to 80% of the luminosity. This trend is expected as H II regions

trace young stars, and it is well known that the co-moving star formation rate density reaches its peak value at $z \approx 2$ (Madu & Dickinson 2014). In general, the average contribution by H II regions is $\sim 20\%$ of $L_{[\text{C II}]}$ over all $z < 4$. For molecular gas, the contribution is on average $\lesssim 10\%$ with a maximum at $z = 0$. In both the molecular and H II regions phases we obtain higher fractional contributions to $L_{[\text{C II}]}$ at higher SFR. This confirms the results found by Olsen et al. (2015) and in Paper I that the contribution of a given phase to $L_{[\text{C II}]}$ depends on the global SFR of the galaxy.

These predictions are not in agreement with recent results from Tarantino et al. (2021) in resolved regions of two local galaxies (M 101 and NGC 6946) where the ionised gas contribution to $L_{[\text{C II}]}$ is negligible (average upper limit of 12%). This disagreement in the ISM phases may be related to the spatial constraints of the observations, as they focus on the arms regions of galaxies where denser neutral gas is expected. For example, Pineda et al. (2018) estimated the $L_{[\text{C II}]}$ contribution coming from different regions inside M 51. They found that the region between the arms in M 51, where the diffuse ionised gas is expected to be located, is approximately 20% of the total $L_{[\text{C II}]}$, compared with $\sim 80\%$ that comes from the arms and the nucleus. In our model, we calculate the global properties of galaxies (in a 30 pkpc aperture), and thus we expect a higher contribution from the diffuse gas, as this ISM phase can cover more extended regions throughout a galaxy. The information from the diffuse phases may therefore be missing when regions close to the arms of disk galaxies are observed. In general, contributions from different phases will depend on the scales over which we observe the galaxies (Tarantino et al. 2021).

It is important to note that our model seems to overpredict the contribution of the ionised phases (DIG + H II regions) for the RECAL-L0025N0752 simulation. In Fig. 5, we examine the relation between the ionised phases to [C II] as a function of metallicity ($12 + \log(\text{O}/\text{H})$). We compare the median predictions of REF-L100N1504 and RECAL-L0025N0752 with the relationship obtained by Cormier et al. (2019), based on the data from their work and Croxall et al. (2017), where at a higher metallicity there is a higher contribution to $L_{[\text{C II}]}$ from the ionised phase. For REF-L100N1504, we estimate fractional contributions $\sim 10\%$ higher than those inferred from the Cormier et al. (2019) fitting function, although at $z = 0$ our predictions can be 40% lower for higher metallicities. In RECAL-L0025N0752 we see that the fractional contributions are always above the empirical fitting function, especially at $z = 1$ and $z = 2$, by around 40%. This means that there may be an overestimation in the ionised component of the RECAL-L0025N0752 luminosities.

The simulations and observations presented in Fig. 5 are in any case difficult to compare. The simulated galaxies may not have the same metallicity calibration as the observed metallicities in Croxall et al. (2017) and Cormier et al. (2019), and the method by which fractional contributions of the ionised gas are calculated may be different. Nonetheless, in general, we find that the contribution of the ionised phase to [C II] increases with increasing metallicity, as observed by Cormier et al. (2019).

3.2. [N II] 122 and 205 μm

3.2.1. The SFR– $L_{[\text{N II}]}$ relationship

The emission lines at 122 and 205 μm of [N II] are commonly used to trace ionised gas phases around neutral clouds, because its ionisation potential is only slightly above that of hydrogen. These lines are also used to disentangle the ionised gas contribu-

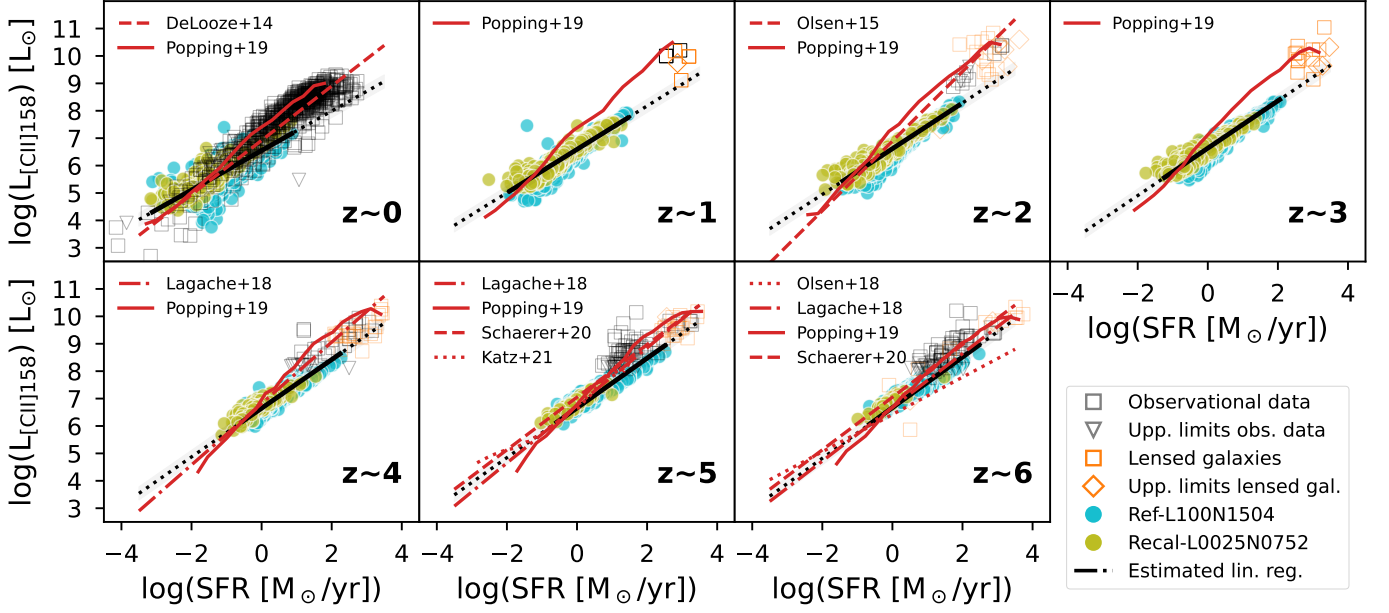


Fig. 2. SFR– $L_{[\text{C II}]}$ relation for all redshift slices used in this work. We compare the obtained relations from the EAGLE simulations REF-L100N1504 and RECAL-L0025N0752 with predictions from other simulations (Olsen et al. 2015, 2018; Katz et al. 2022), semi-analytic models (Lagache et al. 2018; Popping et al. 2019) and linear relations derived from observations (De Looze et al. 2014; Schaerer et al. 2020). Linear relations inferred from our models are shown as black solid lines over the dynamic range covered by the simulations and extrapolated to lower and higher SFRs as black dotted lines, with the grey shaded area representing the 1σ error. Collections of observational data (Appendix A) are plotted as grey squares for detections and as grey triangles for upper limits. For lensed galaxies, the markers are plotted in and the upper limits that affect both the SFR and luminosity are plotted as diamonds.

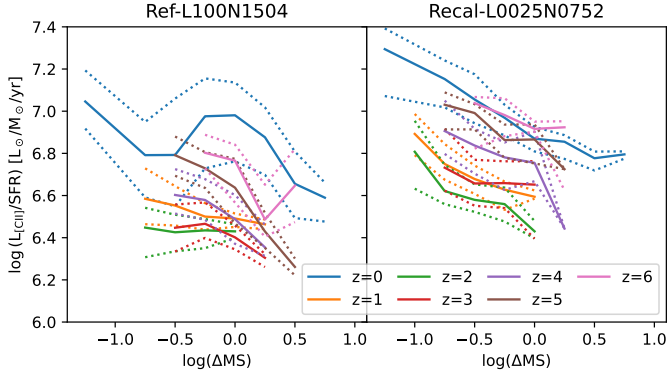


Fig. 3. The ratio $[\text{C II}]/\text{SFR}$ as a function of the offset from the star-forming main-sequence ΔMS for the simulations REF-L100N1504 (left) and RECAL-L0025N0752 (right). We show the median values of the different redshifts (solid lines) and their 25th and 75th percentiles (dotted lines). We only show the bins with more than 3% of the total sample for the respective simulation.

tion to the $[\text{C II}]$ luminosity (e.g. Goldsmith et al. 2015; Ferkinhoff et al. 2015; Pavesi et al. 2016; Croxall et al. 2017; Cormier et al. 2019; Langer et al. 2021), as we do in this work. The relationship of these lines with SFR has been explored in the local Universe (e.g. Herrera-Camus et al. 2016; Zhao et al. 2016a); however, at higher redshifts we have very little observational data, especially for the $122\mu\text{m}$ line. Due to this lack of data at $z > 0$, we focus here on the $[\text{N II}] 205\mu\text{m}$ line. We present $[\text{N II}]$ luminosities at $205\mu\text{m}$ as a function of SFR in Fig. 6. We compare our results with the linear relationships in the local Universe estimated by Zhao et al. (2016a), Herrera-Camus et al. (2016) and Mordini et al. (2021). For the relation of Herrera-Camus

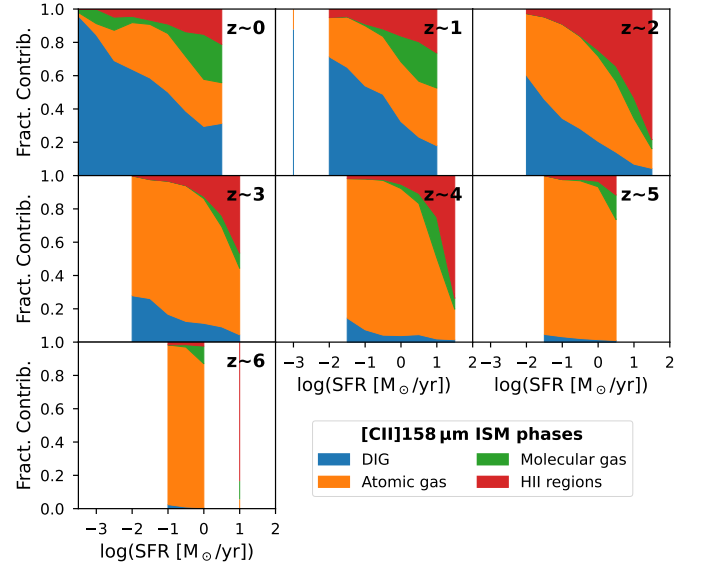


Fig. 4. Contribution from the different ISM phases for the $[\text{C II}]$ emission line in RECAL-L0025N0752. The regions define the DIG (blue), neutral atomic gas (orange), dense molecular gas (green) and HII regions (red).

et al. (2016, eq. 10), we assume the values of the collisional excitation coefficients from Tayal (2011), and abundances close to solar. For the relation of Mordini et al. (2021), we use the sample of AGN galaxies assuming the conversion from infrared luminosities (L_{IR}) to SFR of Kennicutt & Evans (2012). We use the AGN sample in Mordini et al. (2021) as those galaxies also

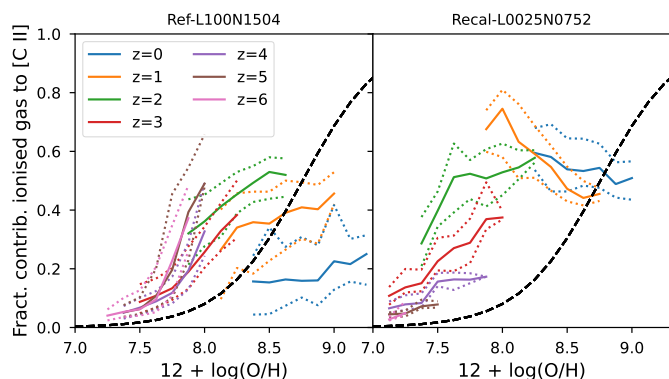


Fig. 5. Contribution of the ionised gas phase to [C II]. We show the median values of the different redshifts (solid lines) and their 25th and 75th percentiles (dotted lines) with respect to the fit to the observational data made by Cormier et al. (2019, black dashed line). In the left panel, we show the predictions of REF-L100N1504 while in the right panel we show the predictions of RECAL-L0025N0752. We only show the bins with more than 5% of the total sample of galaxies for the respective simulation.

follow the relation between SFR and the luminosity of the PAH feature at $6.2 \mu\text{m}$ (see their Fig. 6).

At $z = 0$, the luminosity predictions of [N II] follow a similar relationship to the observational relations of Zhao et al. (2016a) and Mordini et al. (2021). A potential reason for the difference of one to two orders of magnitude with respect to the Herrera-Camus et al. (2016) relation is that the assumption of solar abundances is incorrect². If we assume an abundance below solar in the Herrera-Camus et al. (2016) relation, the relation is closer to our model. At $z = 1$ and $z = 2$ our model is consistent with the upper limits of the observational data. At higher redshifts, $3 < z < 6$, our models agree with the observations, although the range of $L_{[\text{N II}]}/\text{SFR}$ in the observations is larger than the estimations (almost 0.5 dex at $z = 4$). Most of the data at these redshifts come from the work of Cunningham et al. (2020), who observed 40 gravitationally lensed galaxies with the Morita Atacama Compact Array (ACA) of ALMA. The luminosities of these galaxies depend strongly on the lensing magnification factor, which could create a large scatter in the inferred luminosities (due to uncertainties in the assumed lensing model), as observed in the orange data points. Our model shows a good agreement with the observations, including the lensed galaxies after correction for magnification.

3.2.2. Contribution to $L_{[\text{N II}]}$ from each ISM phase

In Fig. 7, we show the contribution of the different phases of the ISM to the [N II] line at $205 \mu\text{m}$. The luminosity of this line comes mainly from the two ionised phases (DIG and H II regions), as expected from observations (e.g. Langer et al. 2021). Interestingly, the relative dominance of these two phases seems to change with redshift and SFR. At higher SFR most of the luminosity comes from H II regions, while at low SFR, most of the luminosity comes from the DIG phase. The DIG can contribute significantly to the luminosity, which is clearer at lower SFR when there are not so many H II regions. In the local Universe, the contribution from the DIG dominates ($\sim 80\%$) over the

² Compared to the relations of Zhao et al. (2016a) and Mordini et al. (2021), the N/H abundance that best matches the data is between the values of 0.03 and 0.16 with respect to solar abundance.

contribution from H II regions. At higher redshifts, $1 < z < 4$, the contribution of the two phases is split relatively evenly. At $z > 5$, H II regions dominate the line emission. In this redshift range, at the highest SFRs, H II regions contribute significantly more than the DIG. The transition point between the phases (the SFR where DIG contributes less than 50% and H II regions more than 50%) is around $1 M_{\odot} \text{yr}^{-1}$ at $z = 0$ and decreases to $0.1 M_{\odot} \text{yr}^{-1}$ at $z = 6$. There is also a very small contribution from the atomic phase ($< 4\%$) at some redshifts, but this is negligible compared to the ionised phases.

3.3. [O I] 63 and 145 μm

3.3.1. The SFR– $L_{[\text{O I}]}$ relationship

The [O I] emission lines at 63 and $145 \mu\text{m}$ trace warm gas in neutral clouds and are commonly detected in galaxies in the local Universe (Malhotra et al. 2001). However, the line at $145 \mu\text{m}$ is fainter than the $63 \mu\text{m}$ line due to its lower spontaneous decay rate and higher upper level energy (Goldsmith 2019). As we did with [N II], here we focus on the results of the brighter line of [O I], i.e., the emission line at $63 \mu\text{m}$.

In Fig. 8 we present predictions of [O I] $63 \mu\text{m}$ luminosity as a function of SFR at different redshifts. Our model at $z = 0$ agrees with the local Universe relationships of De Looze et al. (2014) and Mordini et al. (2021). For the relation of Mordini et al. (2021), we use the sample of star-forming galaxies assuming the conversion from L_{IR} to SFR of Kennicutt & Evans (2012). At $z > 1$, extrapolation of the linear fits to our model predictions are consistent with the observational upper limits. There are only a few detections at $z = 2$, $z = 3$ and $z = 6$ that can be directly compared with our predictions. There are seven detections in the $z = 2$ bin, of which five are > 0.5 dex from the extrapolated linear fit. However, all of these galaxies are gravitationally lensed (Brisbin et al. 2015), and no corrections were applied to correct for lensing because the magnification factors were unknown (see also Zanella et al. 2018). Therefore, it is reasonable to assume that these five measurements should be treated as upper limits. In the other redshift bins, we observe a very good agreement with the linear relationship because the lensing magnification has been taken into account (Rigopoulou et al. 2018; Zhang et al. 2018; Rybak et al. 2020).

Other numerical models, not shown in the plots, also predict the [O I] $63 \mu\text{m}$ line and show similar results. For example, Olsen et al. (2018) predict the emission of 30 simulated galaxies at $z = 6$ in the MUFASA cosmological simulation. All of their galaxies have $\text{SFR} \sim 10 M_{\odot} \text{yr}^{-1}$ and $L_{[\text{O I}]} \sim 10^8 L_{\odot}$, very similar to the estimations of the REF-L100N1504 simulation. However in an updated model, Olsen et al. (2021) use the SIMBA cosmological simulation at $z = 0$, and their predicted [O I] $63 \mu\text{m}$ luminosities are 1.2 dex above the De Looze et al. (2014) relation shown in Fig. 8. This contrasts with our model, which exhibits better agreement with the linear fits of De Looze et al. (2014) and Mordini et al. (2021) at $z = 0$, with a difference of ~ 0.5 dex at $\log(\text{SFR}[M_{\odot} \text{yr}^{-1}]) = 1$. We conclude that the model predictions presented in this work provide a better match with observations across a wide range of redshifts than previous models that only focus on a single redshift slice.

3.3.2. Contribution to $L_{[\text{O I}]}$ from each ISM phase

Contributions to the [O I] $63 \mu\text{m}$ line come mainly from neutral clouds, i.e., neutral atomic gas and dense molecular gas, as shown in Fig. 9. At $z = 0$, the contribution to $L_{[\text{O I}]}$ from molec-

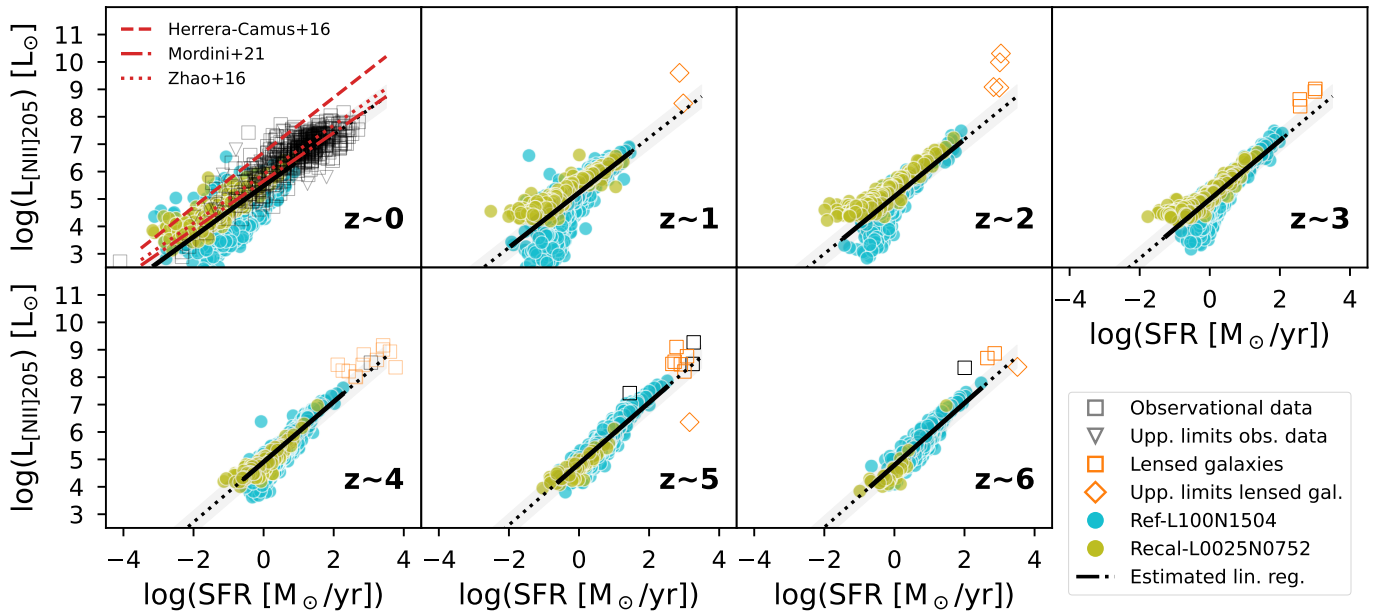


Fig. 6. As Fig. 2 for the [N II] 205 μm line. We present the linear relations estimated by Zhao et al. (2016a), Herrera-Camus et al. (2016) and Mordini et al. (2021) at $z = 0$.

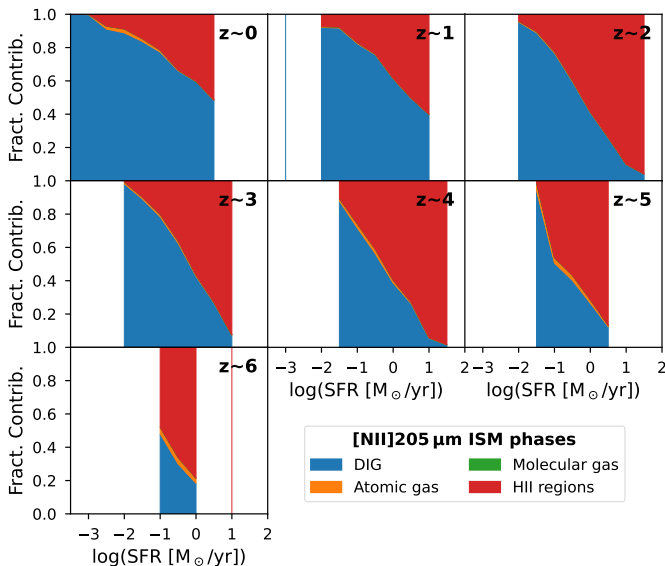


Fig. 7. Contribution from the different ISM phases to the [N II] emission line at 205 μm in RECAL-L0025N0752. Colour-coding is the same as in Fig. 4

ular gas is $\sim 40\%$ while for atomic gas it is $\sim 39\%$. These percentages change with redshift: the contribution from molecular gas decreases and from atomic gas increases with increasing redshift. At $z = 2$ the percentages are $\sim 7\%$ and $\sim 85\%$, respectively, while at $z = 4$ they are $\sim 1\%$ and $\sim 98\%$. The contributions from the other phases are negligible, especially for the HII regions. On average the contribution from the DIG is less than 10%; however, it can be very high ($> 80\%$) in galaxies with very low SFR ($< 10^{-2} M_{\odot} \text{yr}^{-1}$) in the local Universe. At $z \geq 3$, the molecular fraction, which is calculated from the line luminosity in the region defined by the radius at which the transition from atomic to molecular H occurs, in the Plummer profile (Equation 31 in Paper I) is very low. At those redshifts, even though the average

density of the neutral cloud is higher than in the local Universe, the ISRF is also high, which causes the dominant emission to come from the atomic gas instead of the molecular gas. These results support the understanding that the [O I] 63 μm line originates in warm neutral environments (Malhotra et al. 2001; Goldsmith 2019) even in high- z galaxies ($z \sim 6$).

3.4. [O III] 52 and 88 μm

3.4.1. The SFR- $L_{[\text{O III}]}$ relationship

The [O III] emission lines at 52 and 88 μm are the best tracers of ionised gas in the FIR. These lines may be used as SFR tracers as they come mainly from young stars (e.g Ferkinhoff et al. 2010; De Looze et al. 2014; Inoue et al. 2014; Harikane et al. 2020; Yang & Lidz 2020; Yang et al. 2021a). The [O III] 88 μm line has become very important as it may be brighter than the [C II] 158 μm line in galaxies close to the reionisation epoch ($z \geq 7$, Inoue et al. 2014, 2016; Bouwens et al. 2021). As in previous sections, we focus here on the results of only one of the [O III] lines, the [O III] 88 μm line, as we have more observational data for this line. In Fig. 10 we present the [O III] 88 μm luminosities as a function of SFR. We compare the predictions from the EAGLE simulations REF-L100N1504 and RECAL-L0025N0752 with observations of individual galaxies and linear relationships between [O III] and SFR derived from observations (De Looze et al. 2014; Harikane et al. 2020; Mordini et al. 2021) and numerical models (Olsen et al. 2018; Katz et al. 2022; Kannan et al. 2021).

Our predicted SFR- $L_{[\text{O III}]}$ relationships largely agree with observations, although it seems that our predicted relationship is steeper than some relations found in the literature. At $z = 0$, we compare our model with the predictions of De Looze et al. (2014) and Mordini et al. (2021). For the relation of Mordini et al. (2021), we use the sample of star-forming galaxies assuming the conversion from L_{IR} to SFR of Kennicutt & Evans (2012). Both observational relationships appear to have slopes flatter than our model, separated by about an order of magnitude at SFR = $10 M_{\odot} \text{yr}^{-1}$. The reason for this difference is that

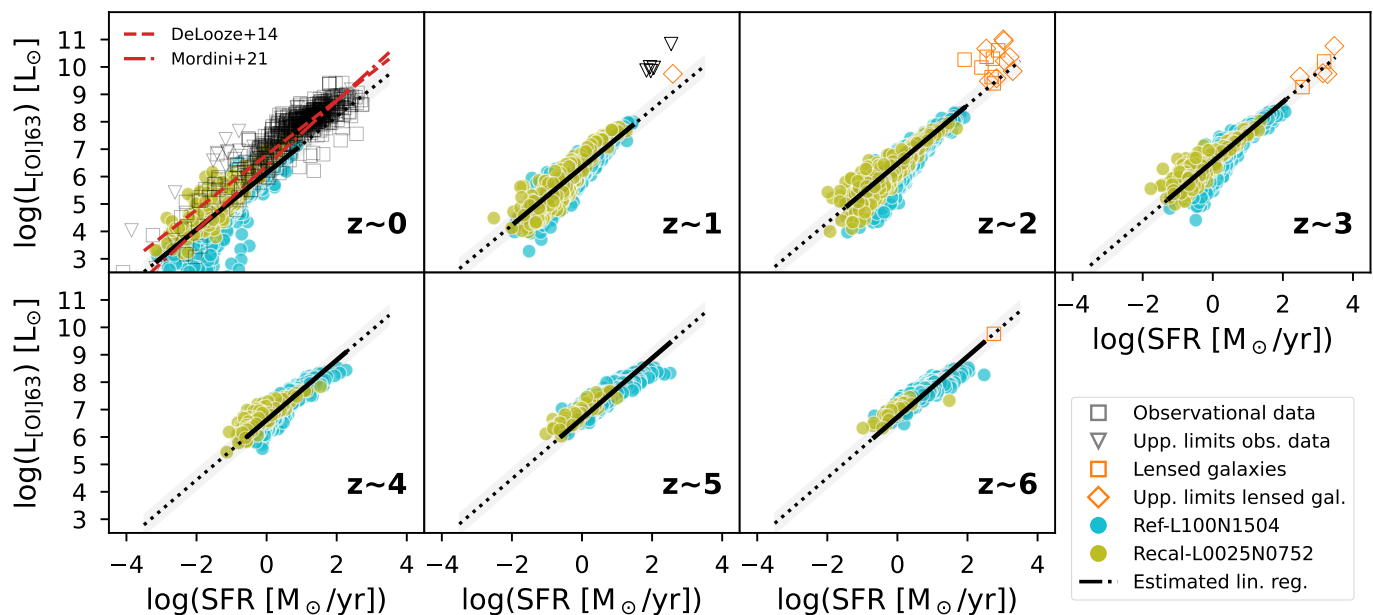


Fig. 8. Similar to Fig. 2 but for the [O I] 63 μm line. We present the linear relations estimated by De Looze et al. (2014) and Mordini et al. (2021) at $z = 0$.

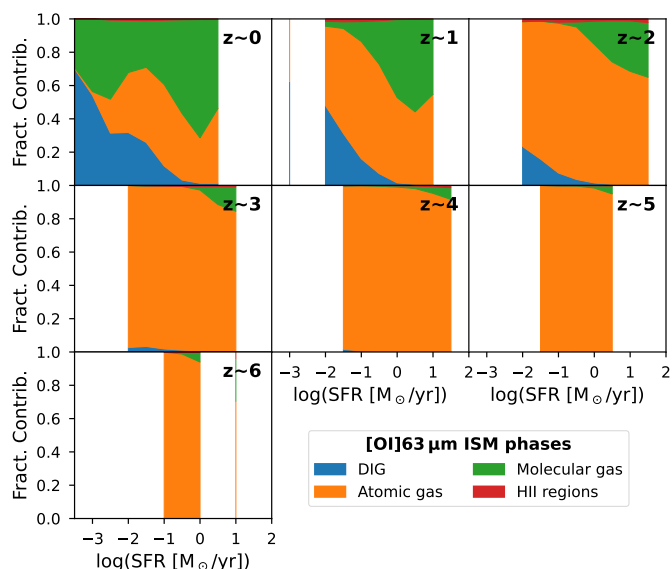


Fig. 9. Contribution from the different ISM phases to the [O I] emission line in RECAL-L0025N0752. Colour-coding is the same as in Fig. 4.

at low SFRs, our luminosity predictions coming from HII regions drop off sharply for both simulations (as we will discuss in the next subsection), leading to a steep slope even though our predicted $L_{[\text{O III}]}$ values agree with the observational data at $\text{SFR} = 1 \text{ M}_{\odot} \text{ yr}^{-1}$.

At $z = 2-4$, due to the small sample size in the observational datasets, it is very difficult to properly assess the level of agreement between the observations and our model predictions. In some cases, the observations agree well with the extrapolation of our predicted $\text{SFR}-L_{[\text{O III}]}$ relations, with a few exceptions. For example, the galaxy located 1.1 dex below the extrapolation at $z = 4$ is AzTEC 1 (Tadaki et al. 2019). The discrepancy in this galaxy is not related to gravitational lensing, but rather this galaxy has a very low $[\text{O III}]/[\text{C II}]$ ratio compared with SPT-

S J041839-4751.8, a galaxy that closely follows our relation (De Breuck et al. 2019). This means that this galaxy may be an outlier and very different physical conditions can shift its position in the $\text{SFR}-L_{[\text{O III}]}$ relation, as we discuss in Sect. 4.

At $z = 5$, we compare our results with those of Katz et al. (2022), which show a similar slope but lower $L_{[\text{O III}]}$ by ~ 1.3 dex. The same model was used to calculate $L_{[\text{O III}]}$ at $z = 6$, showing that their predictions, together with the models of Olsen et al. (2018), underestimate $L_{[\text{O III}]}$ compared with observations by 0.7 dex at $\text{SFR} \sim 100 \text{ M}_{\odot} \text{ yr}^{-1}$. This is not the case with our model: it agrees very well with the observations and with the linear relation from Harikane et al. (2020), with a difference of 0.2 dex at $\text{SFR} \sim 100 \text{ M}_{\odot} \text{ yr}^{-1}$. It is also interesting to note that the numerical results of Kannan et al. (2021) are very similar to those presented in this work, with the difference of a slightly higher slope in their work, which gives a difference of 0.4 dex at $\text{SFR} \sim 10 \text{ M}_{\odot} \text{ yr}^{-1}$.

3.4.2. Contribution to $L_{[\text{O III}]}$ from each ISM phase

In Fig. 11 we show the contribution of the ISM phases to $L_{[\text{O III}]}$, of which the ionised ISM is the only contributor, as expected. The dominant contributor to $L_{[\text{O III}]}$ are the HII regions at most redshifts. However at $z = 0$, the emission coming from the HII regions drops sharply when the SFR decreases. The reason for this sharp drop is the low ionising photon flux coming from the star SPH particles in the simulated galaxies at low SFR. This sets the [O III] line luminosities from the HII regions to almost negligible values compared to the DIG, which explains the trend observed in $z = 0$. At $z = 1$, the lack of ionising photon flux affects galaxies less than at $z = 0$, and at these redshifts the HII regions dominate (72%) over the DIG (28%). For redshifts from $z = 2$ to $z = 6$ the contribution from the HII regions changes from 85% to 99%.

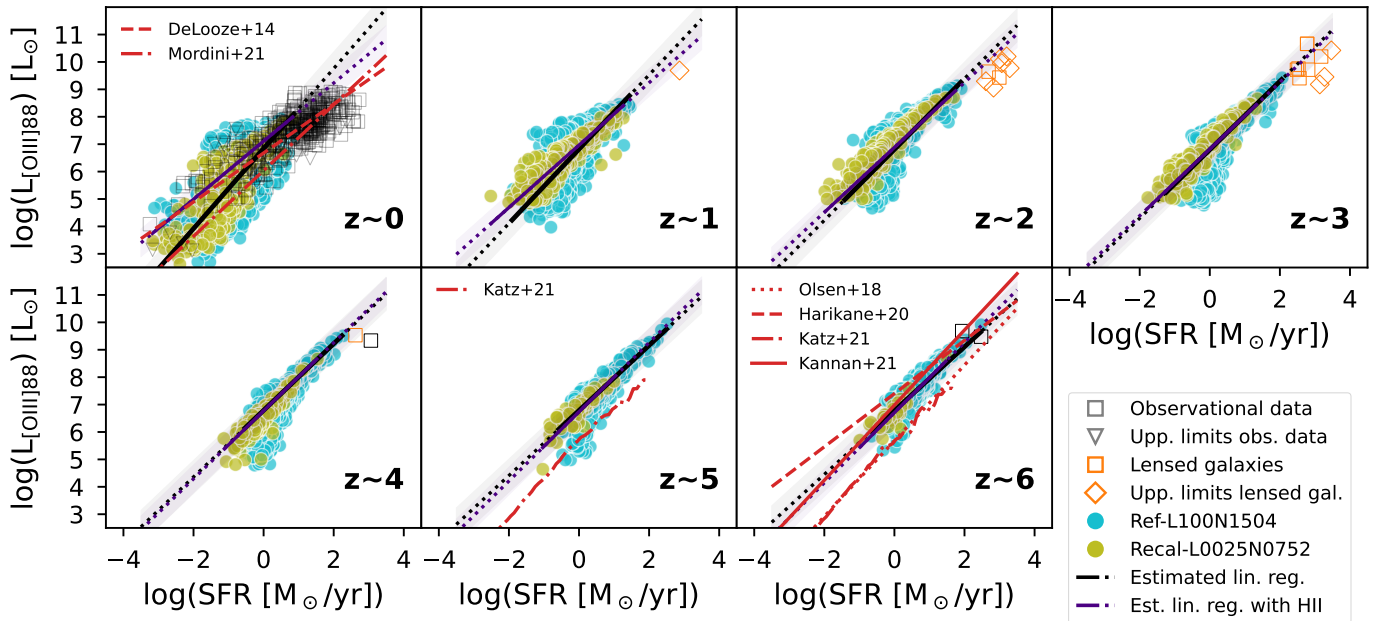


Fig. 10. As Fig. 2 for the [O III] 88 μm line. We compare the obtained relations from the EAGLE simulations with relations derived from simulations (Olsen et al. 2018; Katz et al. 2022; Kannan et al. 2021) and observations (De Looze et al. 2014; Harikane et al. 2020; Mordini et al. 2021). Linear relations inferred from our models using only H II regions are shown as indigo solid lines over the dynamic range covered by the simulations and extrapolated to lower and higher SFRs as indigo dotted lines, with the shaded area representing the 1σ error (see Appendix C).

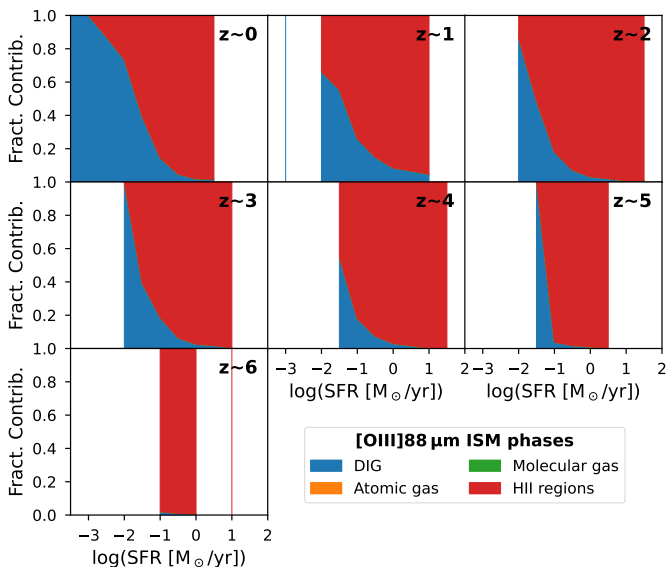


Fig. 11. Contribution from the different ISM phases for the [O III] emission line in RECAL-L0025N0752. Colour-coding is the same as in Fig. 4.

3.5. [N III] 57 μm

3.5.1. The SFR– $L_{[\text{N III}]}$ relationship

The [N III] emission line at 57 μm is very similar to the [O III] 88 μm emission line, due to its excitation properties (Table 1). Both trace H II regions, with the difference that [N III] is fainter in galaxies with metallicities below solar (e.g. Nagao et al. 2011; Rigopoulou et al. 2018). The relationship between the SFR and $L_{[\text{N III}]}$ is less well known than the other FIR emission lines presented in this work. In Fig. 12, we present the SFR– $L_{[\text{N III}]}$ relationship. We compare predictions from the EAGLE simulations

with the observational sample and the linear relation at $z = 0$ by Mordini et al. (2021) in AGN galaxies assuming the conversion from L_{IR} to SFR of Kennicutt & Evans (2012), as we did in the case of [N II].

At $z = 0$, our model predictions agree with the observations, with a mean offset of 0.2 dex, as they are inside the observational scatter for the overlapping SFR range. However, the $L_{[\text{N III}]}$ predictions have the same problem as the $L_{[\text{O III}]}$ predictions: the low ionising photon flux coming from SPH star particles in simulated galaxies at low SFR. This leads to a steeper relation of $L_{[\text{N III}]}$ with SFR than that of Mordini et al. (2021), which follows the other observational results. At $z \geq 1$, even though there is not much information, we find that the extrapolation of our linear fit is consistent with the upper limits and detections in two galaxies at $z \approx 2$ (H-ATLAS J091043.1-000321, Lamarche et al. 2018) and $z \approx 3$ (HERMES J105751.1+573027, Rigopoulou et al. 2018). These two galaxies are magnified by around an order of magnitude (magnification factors of 11.5 and 10.9, respectively), therefore the agreement with our model, after applying the magnification correction, shows that the slope of the linear relationship may be correct for these redshifts.

3.5.2. Contribution to $L_{[\text{N III}]}$ from each ISM phase

The contributions of the ISM phases to the [N III] 57 μm emission line are very similar to the contributions of the phases to the [O III] 88 μm line (Fig. 11), as shown in Fig. 13. The main difference resides in the exact percentages between the two dominant ionised ISM phases (DIG and H II regions). At $z = 0$, the contributions of the DIG and H II regions to $L_{[\text{N III}]}$ are 38% and 62%, respectively. At higher redshifts these percentages change to 15% and 85% at $z = 2$, 8% and 91% at $z = 4$, respectively. Finally, at $z = 6$ the H II regions are responsible for almost all the $L_{[\text{N III}]}$.

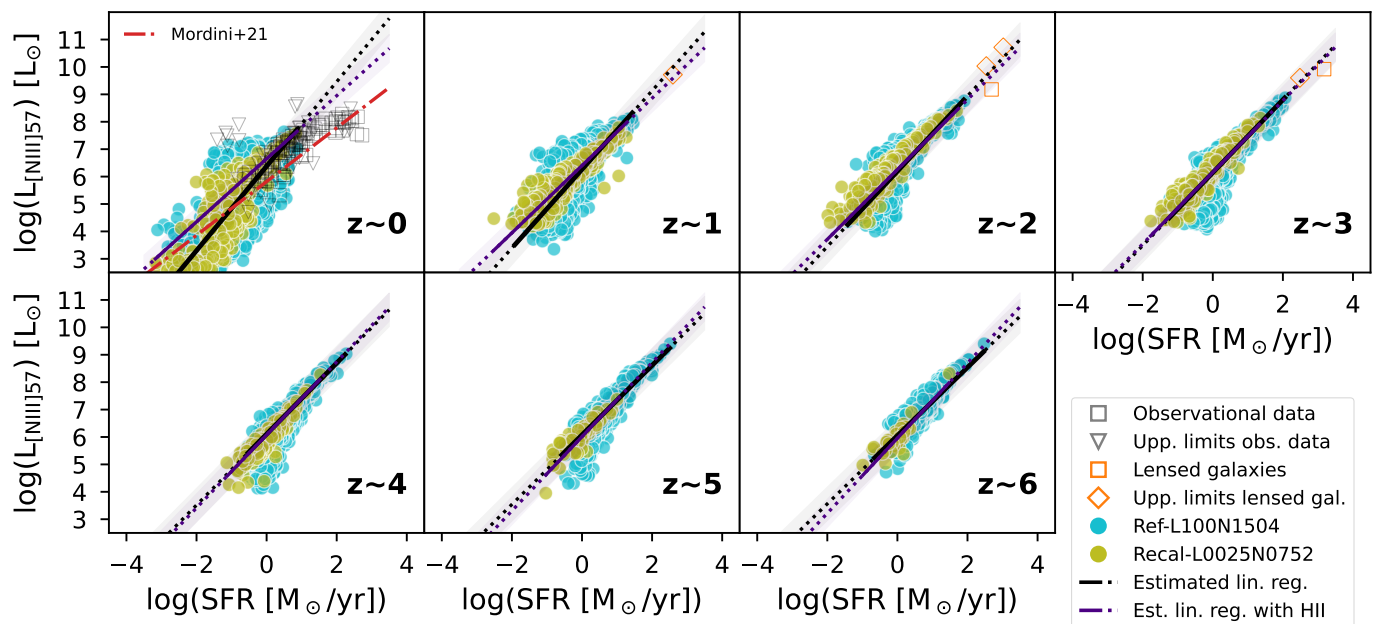


Fig. 12. As Fig. 10 for the [N III] 57 μm line. We present the linear relations estimated by Mordini et al. (2021) at $z = 0$.

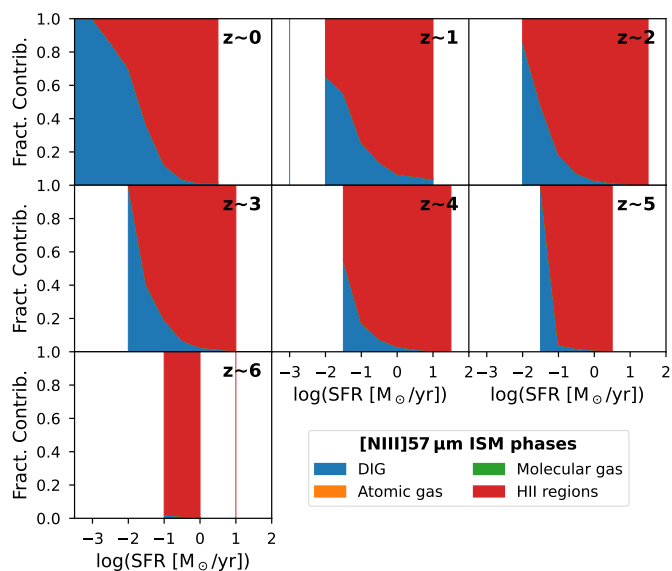


Fig. 13. Contribution from the different ISM phases for the [N III] emission line in RECAL-L0025N0752. Colour-coding is the same as in Fig. 4.

3.6. Summary of FIR line luminosities

The relationships of the SFR with the different FIR line luminosities presented in Sects. 3.1–3.5 depend on redshift (Figs. 2, 6, 8, 10 and 12). We assume a potential redshift dependency in the linear fits of our line predictions (Eq. C.1), which shows a good agreement with the observations. Nonetheless, we want to quantify how these FIR lines and their dependence on SFR evolve with redshift. To do this, we plot in Fig. 14 the ratio between luminosity and SFR (L/SFR) versus redshift for the eight lines modelled in this work.

First, we compare the results of the two sets of simulations REF-L100N1504 and RECAL-L0025N0752. Taking into account the scatter of the predictions, we find a good agreement between

them, even though some of the physical properties of galaxies in the simulations are different, as we discuss in Sect. 5.

The evolution of the L/SFR ratio is almost flat for most FIR lines at $z \geq 4$. At lower redshifts, $1 < z < 3$, however, there are drastic changes in the L/SFR ratio. For example, the [O III] lines at 52 and 88 μm have higher L/SFR values at $z = 2$ and then decrease sharply towards $z = 0$, by almost an order of magnitude. The opposite occurs for [C II], where at $z = 2$ the L/SFR ratio has lower values than at other redshifts, although the difference is less than 0.5 dex.

These changes are related to the effects present in galaxies during “cosmic noon”, where the cosmic star-formation history reaches its peak value at $z \approx 2$ and around half of the stellar mass of the local Universe was formed, affecting the different phases of the ISM traced by the FIR lines in Fig. 14 (Madau & Dickinson 2014; Förster Schreiber & Wuyts 2020). This result is expected because the EAGLE galaxies reproduce the observed trend in the SFR density and stellar mass assembly across cosmic time (Furlong et al. 2015) and so the ISM phases evolve accordingly with redshift (Figs. 4, 7, 9, 11 and 13).

The two [O III] lines have a similar shape in Fig. 14, which explains why both lines can be used to constrain gas density and metallicity at high- z (Yang et al. 2021a). The [N II] pair shows a similar behaviour, where the main difference resides in the value of the L/SFR ratio at $z = 0$, although the scatter is especially large at this redshift. This could be important when estimating electron densities from observations from the ratio of these two [N II] lines (Croxall et al. 2017; Langer et al. 2021). Finally, for both [O I] lines, we see a clear difference between the estimated luminosities of the lines of around 1.15 dex over most of the redshift range. This difference of more than an order of magnitude is expected from theoretical models. If the difference in [O I] luminosities is more than 1.15 dex, it may indicate higher kinetic temperatures (> 400 K) and/or lower gas densities ($\leq 10 \text{ cm}^{-3}$) in observations (Goldsmith 2019).

With this information, we can ask which FIR emission line is the best SFR tracer across cosmic time. The FIR line showing the least variation with z is [C II]. However, this tracer may

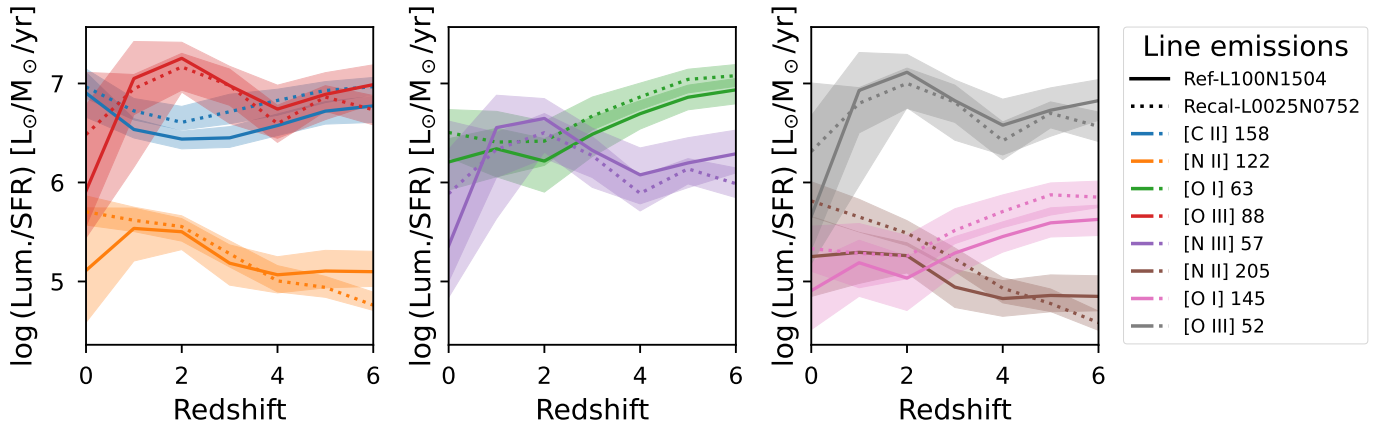


Fig. 14. Evolution of the line luminosity–SFR ratio with redshift for the main FIR lines modelled in this work. We show the median values from RECAL-L0025N0752 (dotted lines) and REF-L100N1504 (solid lines). The shaded regions correspond to the 25th and 75th percentiles.

not be ideal in some cases: observations, analytical models and simulations (e.g. Schaerer et al. 2020; Popping et al. 2019; Carniani et al. 2020) suggest that there might be a weak evolution for the $SFR-L_{[C II]}$ relation with respect to redshift. Our model suggests that there is a slight evolution, although less than for the other lines, as shown by the coefficient c_2 in Table C.1 and Equation C.1. The luminosity evolution may be related to the active star-formation processes that occur in starburst galaxies, as shown in Fig. 3, and in galaxies during “cosmic noon” at $z \approx 2$. The regulation of these star-formation processes is reflected in the changes of the ISM phases (Fig. 4), which tend to be more stable in the case of $L_{[C II]}$.

Another possibility is to use $L_{[O III]}$ as an SFR tracer, since the $[O III]$ lines tend to be equal to or brighter than $L_{[C II]}$ in some redshift ranges (e.g. Arata et al. 2020; Carniani et al. 2020; Vallini et al. 2021; Bouwens et al. 2021; Katz et al. 2022). However, our $L_{[O III]}$ predictions at $z = 0$ may be underestimated for lower SFR (see Sect. 3.4.2), which may explain the decrease in the median value of the L/SFR ratio for these lines. It is also possible to use $L_{[O III]}$ together with $L_{[O I]}$ at $63 \mu m$ as an SFR tracer (Mordini et al. 2021) to balance the neutral and ionised components of the ISM in these lines. Nevertheless, this use would require having access to both luminosities ($L_{[O III]}$ and $L_{[O I]}$) at $z < 4$ to confirm the trends presented in Fig. 14. The $[O I]$ $63 \mu m$ line alone could also be used to trace the SFR, as this line has similar properties to the $[C II]$ line (Katz et al. 2022). For example, in the predictions of Olsen et al. (2018), $[O I]$ is brighter than $[C II]$ at $z = 6$, and therefore is more easily observable. The trend of $[O I]$ being brighter than $[C II]$ is also predicted in this work, confirming the results from Olsen et al. (2018). Therefore, $L_{[C II]}$ may be the best SFR tracer across the entire redshift range of this work ($z = 0-6$), but at high- z other FIR lines such as $[O III]$ and $[O I]$ are also very useful.

4. Diagnostic diagrams using FIR lines

We now examine our predictions of FIR emission line strengths from the EAGLE simulations in the context of diagnostic diagrams. Typically, diagnostic diagrams use emission line ratios that reflect the physical conditions of the ISM. In this work, we focus on two diagnostic diagrams: one that normalises the emission line luminosity with SFR for $[C II]$ and $[O III]$ at $88 \mu m$ (Harikane et al. 2020), and the other that uses the ratios between $[C II]/[O III]$ and $[N II]/[O I]$, based on the $[O III]$, $[N II]$ and $[O I]$

lines at $88 \mu m$, $205 \mu m$ and $63 \mu m$, respectively. With these two diagnostic diagrams we investigate whether these ratios trace physical quantities related to the ISM, such as radiation field and density.

Other line ratios in the FIR are also of great interest for different types of studies (e.g. Sect. 3.3 of Cormier et al. 2015). We therefore make our model predictions for different emission lines of these simulated EAGLE galaxies publicly available, as described in Appendix B. Similar FIR diagnostic diagrams, such as those presented by De Breuck et al. (2019) and Li et al. (2020) are not discussed in this work, but plots are provided as supplementary material³.

4.1. Comparison with observations

We compare our model predictions with the observational dataset of Appendix A and the results from the latest version of the SIGAME framework presented by Olsen et al. (2021). The latest version of the SIGAME framework uses the SIMBA simulations (Davé et al. 2019) with the SKIRT (Camps & Baes 2020) radiative transfer code and CLOUDY (Ferland et al. 2017) to predict line luminosities, similar to this work. The SIGAME predictions come from galaxies in two simulated boxes of 25 cMpc and 100 cMpc volumes in the local Universe, similar to the EAGLE box sizes used in this work. Olsen et al. (2021) find that their $L_{[C II]}$ predictions appear to be an extension to higher SFRs of the model predictions presented in Paper I. However, SIGAME tends to have higher line luminosities relative to the $SFR-L_{[C II]}$ relationship (their Fig. 11). In addition, their 25 cMpc box returns even higher line luminosities up to $\sim 0.5-1.5$ dex of the 100 cMpc box.

In Fig. 15, we compare the $L_{[O III]}/SFR$ and $L_{[C II]}/SFR$ ratios of our model predictions with the observational data and the SIGAME predictions. For the local Universe, our predictions share a similar range of values with the observational data, which tends to be in the range between $6.5 < \log(L_{[C II]}/SFR) < 7.6$ and $5.8 < \log(L_{[O III]}/SFR) < 7.6$. However, most of the simulated galaxies tend to be above ($\log(L_{[O III]}/SFR) > 6.8$) or below ($\log(L_{[O III]}/SFR) < 6.0$) the observational data. In contrast, SIGAME predictions tend to have very high $[C II]$ luminosities, which shifts most of the SIGAME simulated galaxies

³ Zenodo repository at <https://doi.org/10.5281/zenodo.6576202>

to $\log(L_{[\text{C II}]}/\text{SFR}) > 7.5$ values, with the SIGAME values peaking an order of magnitude higher than the observed galaxies and our simulated ratios. This difference is expected from the comparisons presented by [Olsen et al. \(2021\)](#). As noted above, the SIGAME predictions of $L_{[\text{C II}]}/\text{SFR}$ are higher than those described in [Paper I](#), which are similar to those in this work. The SIGAME $L_{[\text{O III}]}/\text{SFR}$ values seem to be similar to our predictions, with values between $6.0 < \log(L_{[\text{O III}]}/\text{SFR}) < 8$.

At $z > 0$, there are very few observed galaxies with which we can compare our results. At $z = 2$, we only have two measurements for one galaxy: H-ATLAS J091043.0-000322. These two measurements come from *Herschel* observations following different data reduction methods (i.e. pipeline versions) in [Zhang et al. \(2018\)](#) and [Lamarche et al. \(2018\)](#). ALMA observations presented by [Lamarche et al. \(2018\)](#) show that the $[\text{C II}]$ luminosity is around half of the *Herschel* measurement (right data point on the panel), but this difference cannot be fully explained. Therefore, we assume that H-ATLAS J091043.0-000322 lies somewhere between the two measurements presented in the $z = 2$ panel, agreeing with the predictions from RECAL-L0025N0752.

At $z = 3$, we have three measurements for SDP 81 ([Valtchanov et al. 2011](#); [De Looze et al. 2014](#); [Zhang et al. 2018](#)) and one for HLock01 ([Rigopoulou et al. 2018](#)). For SDP 81, two of the measurements coincide ([De Looze et al. 2014](#) use the values from [Valtchanov et al. 2011](#)): the empty squares with $\log(L_{[\text{C II}]}/\text{SFR}) \sim 7.6$. The other measurement for SDP 81 comes from [Zhang et al. \(2018\)](#), which is the leftmost point in the $z = 3$ panel. The main difference between the values of [Valtchanov et al. \(2011\)](#) and [Zhang et al. \(2018\)](#) is the different data reduction methods, and therefore we rely on the more recent results of [Zhang et al. \(2018\)](#). Both SDP 81 and HLock01 are close to the model predictions of RECAL-L0025N0752.

At $z = 4$, we have measurements for two galaxies: SPT-S J041839-4751.8 ([De Breuck et al. 2019](#)) and AzTEC 1 ([Tadaki et al. 2019](#)). Our results agree with the location of both objects, a bit to the left of the results from the $z = 0$ galaxies.

Finally, at $z = 6$ we have measurements for two galaxies: [DWV2017b] CFHQ J2100-1715 companion ([Walter et al. 2018](#)) and [MOK2016b] HSC J121137.10-011816.4 ([Harikane et al. 2020](#)). [DWV2017b] CFHQ J2100-1715 companion is in the same region where most of our model predictions are at $z = 6$. In contrast, [MOK2016b] HSC J121137.10-011816.4 falls in the same upper region as SPT-S J041839-4751.8 in the $z = 4$ panel. The latter two galaxies have SFRs around $100 M_{\odot} \text{ yr}^{-1}$ and have $L_{[\text{O III}]}$ higher than their respective companions in their panels. These high SFRs can explain their positions in the diagnostic diagrams. [Harikane et al. \(2020\)](#) presented two other galaxies in the same redshift range for the ratios presented in [Fig. 15](#) besides [MOK2016b] HSC J121137.10-011816.4. Those two galaxies have been removed from the comparison because they have been identified as QSOs.

For the other diagnostic diagram, in [Fig. 16](#), we compare the $[\text{C II}]/[\text{O III}]$ and $[\text{N II}]/[\text{O I}]$ ratios of our predictions with the observational data and SIGAME predictions. For the local Universe ($z = 0$ panel), we observe that our predictions, observational data and SIGAME predictions tend to be grouped in the region between $-0.5 < \log(L_{[\text{C II}]} / L_{[\text{O III}]}) < 1.5$ and $-1 < \log(L_{[\text{N II}]} / L_{[\text{O I}]}) < 1$. The SIGAME predictions match most of the observational data, especially for the 100 cMpc box, although they do not reach the values close to $\log(L_{[\text{C II}]} / L_{[\text{O III}]}) = 0$ and $\log(L_{[\text{N II}]} / L_{[\text{O I}]}) = 0$. The difference between the SIGAME 100 cMpc and 25 cMpc boxes comes from the high $L_{[\text{C II}]}$ that galaxies in the latter box can have, something that we also commented on at the beginning of this section. Our model behaves

similarly to [Fig. 15](#), where most of the observations lie between the two concentration regions for RECAL-L0025N0752, and the REF-L100N1504 agree with the observations. Our estimates with a simple model of the ISM are in the same parameter space as observations. Unfortunately, a completely fair comparison cannot be made because of selection bias in both the observational and simulated galaxies.

Unfortunately, as we are using four FIR emission lines, there are few observational data points to which we can compare at higher redshifts. The only galaxy with all four FIR lines is SPT-S J041839-4751.8 at $z = 4$ ([De Breuck et al. 2019](#)). Our model matches the position of this galaxy in this diagram, similar to the results presented in [Fig. 15](#). The location of this galaxy and most of our predictions at high- z in [Fig. 16](#) seem to coincide with some of the observational data at $z = 0$, which may imply that some physical parameters (e.g. sSFR, metallicity and/or density) in these galaxies will be similar at different redshifts.

The comparison presented in [Figs. 15 and 16](#) show that our model predictions largely match the parameter space of the observational data in the diagnostic diagrams. We conclude that our model predictions can be used to interpret the physical parameters of observed galaxies.

4.2. Physical parameters in diagnostic diagrams

Now, we use the diagnostic diagrams to infer the ISM physical conditions in galaxies. We use the simulation data of all modelled galaxies and compare the sensitivity of the line luminosity-to-SFR ratio to eight physical parameters as estimated in [Paper I](#): gas mass (M_{gas}), stellar mass (M_{*}), metallicity (Z/Z_{\odot}), specific star formation rate (sSFR), interstellar radiation field (ISRF), total hydrogen number density in the neutral clouds ($n(\text{H})_{\text{cloud}}$), external pressure (P_{ext}) and radius of the neutral clouds (R_{cloud}). We divide these physical parameters into seven ranges to compare them with the observational dataset of [Appendix A](#) and, as a reference, our mock data from RECAL-L0025N0752 at $z = 0$.

We begin by presenting the physical parameters in the $L_{[\text{O III}]}/\text{SFR} - L_{[\text{C II}]}/\text{SFR}$ diagnostic diagram in [Fig. 17](#). We note that the impact of almost all the physical parameters is perpendicular to the observational sample. This effect arises because our mock data also tend to be perpendicular to the observational data, especially at $z = 0$. From these physical parameters, we see that most of the predicted galaxies at the upper-left boundary of the observational contour tend to have higher M_{gas} , M_{*} , sSFR, ISRF, $n(\text{H})_{\text{cloud}}$ and P_{ext} , and lower R_{cloud} . In addition, low values of M_{*} do not reach the bottom-right limit of the observational contour, while the metallicity spans all over the observational contours and does not have a clear trend.

[Harikane et al. \(2020\)](#) used the $L_{[\text{O III}]}/\text{SFR} - L_{[\text{C II}]}/\text{SFR}$ diagnostic diagram to explain the physical properties of galaxies at $z = 6-9$ compared with the local Universe. Using simple CLOUDY grids, they found that one of the probable reasons for the location of some of their galaxies in the upper-right region of the diagnostic diagrams was a high ionisation parameter, which is proportional to the ISRF. Their result is similar to what we find from [Fig. 17](#); however, it is also important to compare the diagnostic diagram with our metallicity and density results. In terms of metallicity, [Harikane et al. \(2020\)](#) find that $L_{[\text{O III}]}/\text{SFR}$ decreases with metallicity while $L_{[\text{C II}]}/\text{SFR}$ does not change. We find the same result for $L_{[\text{C II}]}/\text{SFR}$, but the range of change of the $L_{[\text{O III}]}/\text{SFR}$ ratio is not directly dependent on metallicity. In terms of density, [Harikane et al. \(2020\)](#) find that both ratios decrease with density, which we also find for our predictions of $L_{[\text{C II}]}/\text{SFR}$ – but not for $L_{[\text{O III}]}/\text{SFR}$. A simple reason for this discrepancy is

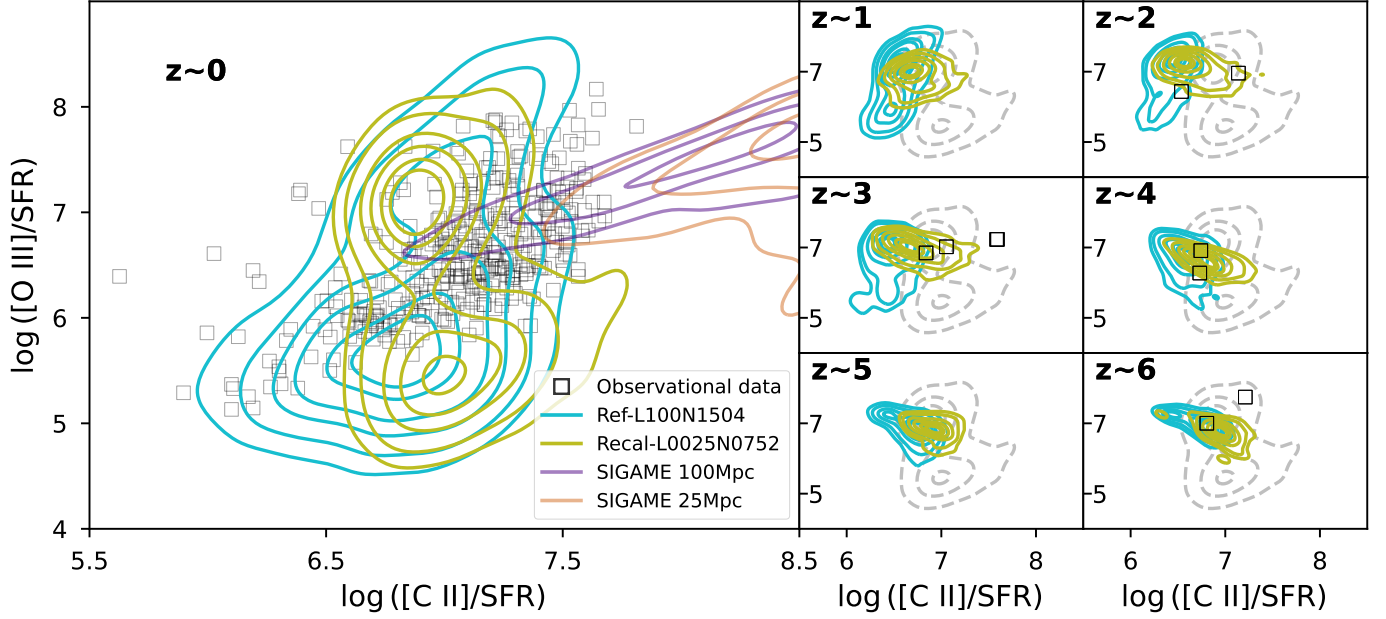


Fig. 15. Diagnostic diagram for the $L_{[\text{O III}]}/\text{SFR}$ and $L_{[\text{C II}]}/\text{SFR}$ ratios, similar to that presented by Harikane et al. (2020). Cyan and olive contours show the model predictions from REF-L100N1504 (cyan) and RECAL-L0025N0752 (olive). We compare with observational data (black squares) and SIGAME predictions (Olsen et al. 2021) for the local Universe in 25 Mpc and 100 Mpc simulation boxes (purple and chocolate contours). All panels with redshifts above zero show the $z = 0$ RECAL-L0025N0752 estimations as grey dashed contours.

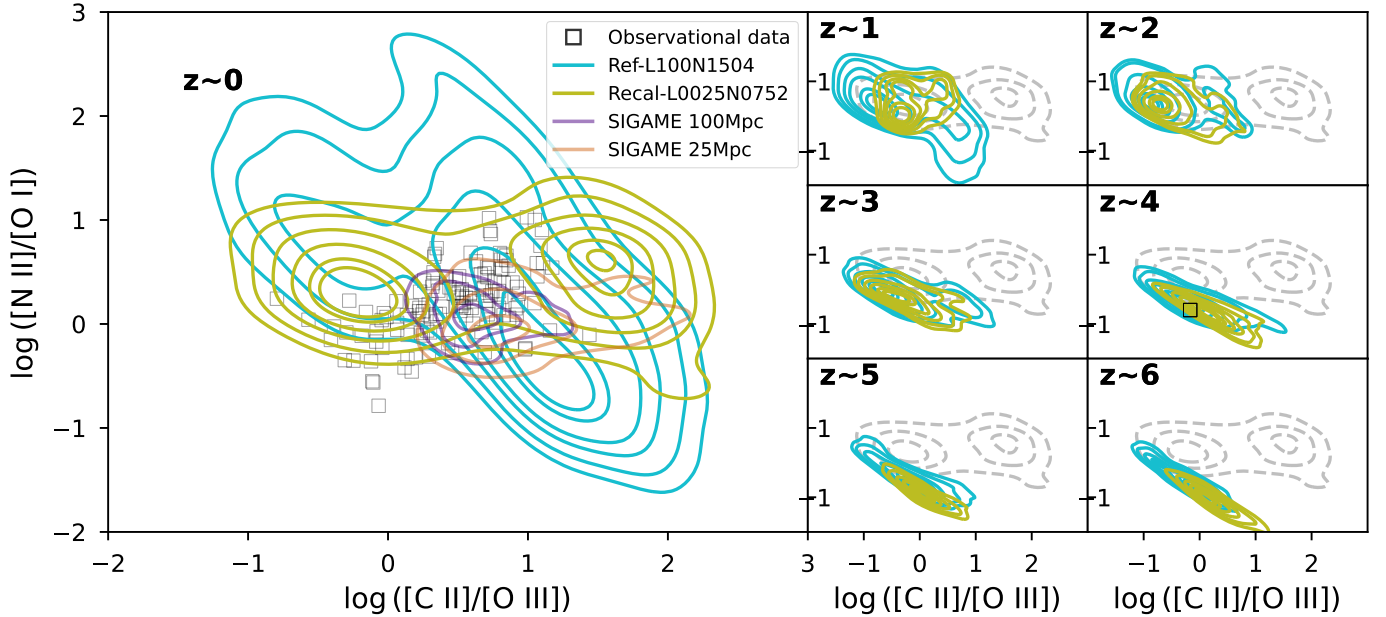


Fig. 16. Diagnostic diagram using four different FIR emission lines comparing the $[\text{C II}]/[\text{O III}]$ ratio against the $[\text{N II}]/[\text{O I}]$ ratio. Colour-codes are the same as in Fig. 15.

that $L_{[\text{C II}]}/\text{SFR}$ depends mainly on density while $L_{[\text{O III}]}/\text{SFR}$ is more dependent on other physical parameters: namely metallicity, sSFR and gas mass.

Figs. 15 and 17 highlight the importance of the $[\text{C II}]$ and $[\text{O III}]$ emission lines in understanding the physical conditions of gas of galaxies, especially by using their ratio, as other recent studies have done (e.g. Harikane et al. 2020; Arata et al. 2020; Carniani et al. 2020; Vallini et al. 2021; Bouwens et al. 2021) and as we show below. We check its correlation with other FIR lines that trace the neutral and ionised gas components, such as the

$[\text{N II}]/[\text{O I}]$ ratio. We present the physical parameters of the diagnostic diagram of the $[\text{C II}]/[\text{O III}]$ vs $[\text{N II}]/[\text{O I}]$ ratios in Fig. 18. In this diagnostic diagram, we note how the physical parameters cross the observational data contours in different ways. Interestingly, the physical parameters in the bottom row panels show a “spoon-like” shape showing that most of the observed galaxies have low to moderate values for the ISRF, $n(\text{H})_{\text{cloud}}$, and P_{ext} , and moderate to high values for the R_{cloud} . The opposite occurs in the region with low $[\text{C II}]/[\text{O III}]$, (i.e. high ISRF, $n(\text{H})_{\text{cloud}}$ and P_{ext} , and low R_{cloud}), which coincides with our predictions

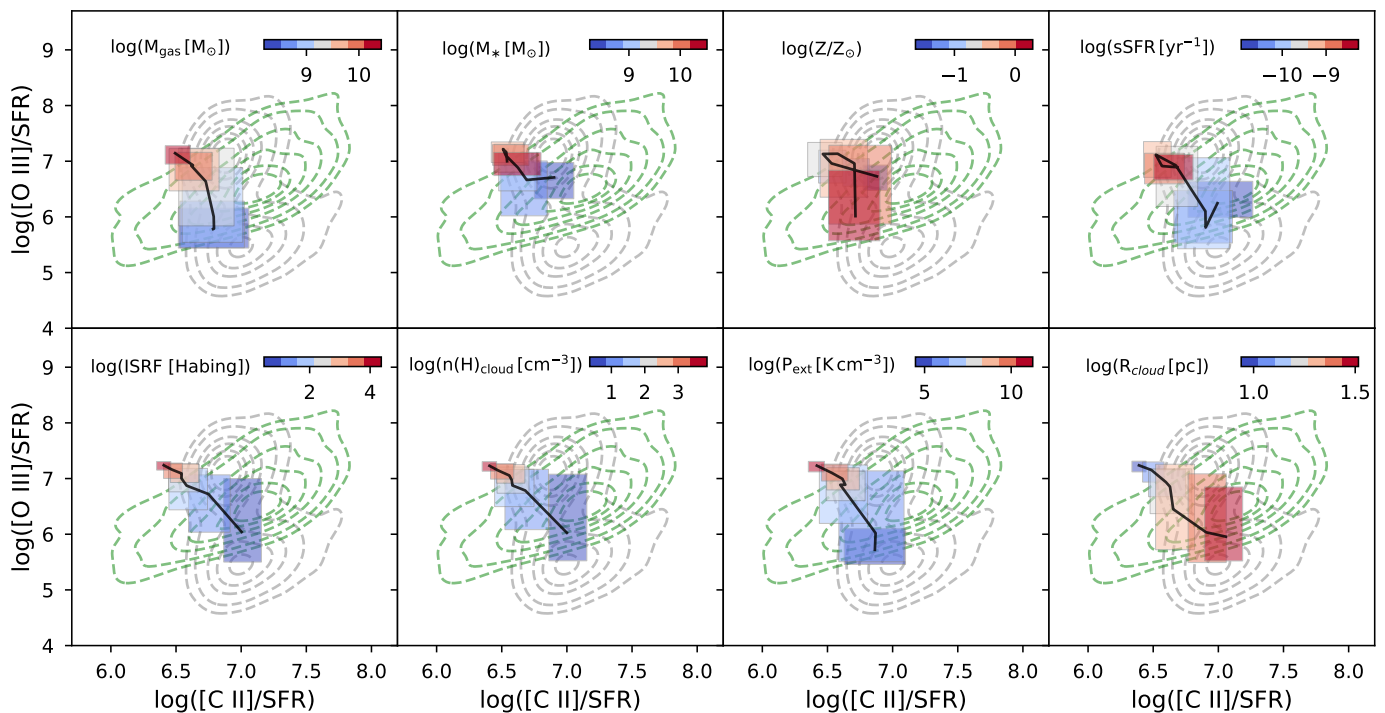


Fig. 17. Physical parameters in the $L_{[\text{O III}]88}/\text{SFR}-L_{[\text{C II}]/\text{SFR}}$ diagnostic plot (see Fig. 15). All panels show the $z = 0$ RECAL-L0025N0752 model predictions as grey dashed contours and the observational data as green dashed contours. In each panel, colour-coded rectangles represent the 25th and 75th percentiles for a given parameter from low (blue) to high (red) values. The solid black lines connect the median values of each rectangle. The scales for all physical parameters are logarithmic.

for high- z galaxies ($z > 3$, in Fig. 16). In terms of mass, M_{gas} is more extended but follows a similar trend to the parameters mentioned above, while M_* does not show a clear trend. The most intriguing trends in the $[\text{C II}]/[\text{O III}]-[\text{N II}]/[\text{O I}]$ diagnostic diagram come from metallicity and sSFR. In terms of metallicity, the $[\text{C II}]/[\text{O III}]$ ratio seems to be a good tracer for metallicities close to solar, while the $[\text{N II}]/[\text{O I}]$ ratio is a good tracer for metallicities below $\log(Z/Z_{\odot}) \lesssim 0.5$, which agrees with some results for high- z galaxies (Arata et al. 2020). In terms of sSFR, both ratios do a good job of separating high and low sSFR of galaxies in a zigzag pattern across the observational sample region. This supports the idea that the $[\text{C II}]/[\text{O III}]$ ratio can be used for starbursting systems (Vallini et al. 2021).

We have shown that both diagnostic diagrams track the behaviour of the physical parameters presented in the simulated galaxies using the luminosities of the main FIR lines. Our model agrees with the observational data in most of the parameter space, and in some cases with other simulations (e.g. SIGAME). Therefore, it is reasonable to expect that the physical model could be used in inferring the physical parameters in FIR diagnostic diagrams to trace different physical parameters.

Comparing our model predictions with new observational data will give an idea of what kind of physical parameters are expected in those galaxies. At the same time, our model can constrain the expected luminosities of FIR lines when no other measurement is available. However, we emphasise that the modelled FIR lines can also be used to study other types of problems. For example, ratios such as $[\text{N II}]/[\text{C II}]$ or other diagnostic diagrams can be used to characterise different types of galaxies (e.g. Ultraluminous infrared galaxies (ULIRGS, where $L_{\text{IR}} > 10^{12} L_{\odot}$) in the local Universe (e.g. Farrah et al. 2013) and at high- z (e.g. Cunningham et al. 2020). Another example is that the ratio between the two $[\text{O III}]$ lines can be used to test the efficiency of

the black hole feedback in galaxies, as was done with the IllustrisTNG simulations (Inoue et al. 2021). Similarly, ratios like $[\text{O III}]/[\text{N III}]$ or $[\text{O III}]/[\text{N II}]$ can be used as a metallicity indicator (e.g. Nagao et al. 2011; Rigopoulou et al. 2018; Fernández-Ontiveros et al. 2021), which will be explored in future studies.

5. Discussion

5.1. Model assumptions

Although our model emission-line luminosities and ratios are in good agreement with observational results and other simulations, our physically motivated model is based on a number of assumptions. The effect of some of these assumptions is generally not visible in these types of predictions due to uncertainty in the observations and our current understanding of some of the physical processes involved. However, these assumptions may be important for models that try to predict the FIR line emission of galaxies, especially at high- z . In this section we highlight the most important assumptions.

For neutral clouds and HII regions, we assume static spherical geometries to describe the densities and temperatures within those environments. This assumption is made for simplicity, although we know that these structures may not be spherical. Physical processes such as radiation destroy spherical geometries (Deharveng et al. 2010; Peñaloza et al. 2018), which may lead to rough or incorrect line luminosity predictions (Decataldo et al. 2020). However, approximations using mass distributions (Eq. 15 in Paper I) may smooth out these differences, since cloud masses follow scaling relations that seem to be valid for observations at different redshifts (Dessauges-Zavadsky et al. 2019).

A problem with our modelled line luminosities from HII regions is that we assume a fixed density ($\sim 30 \text{ cm}^{-3}$). We can in-

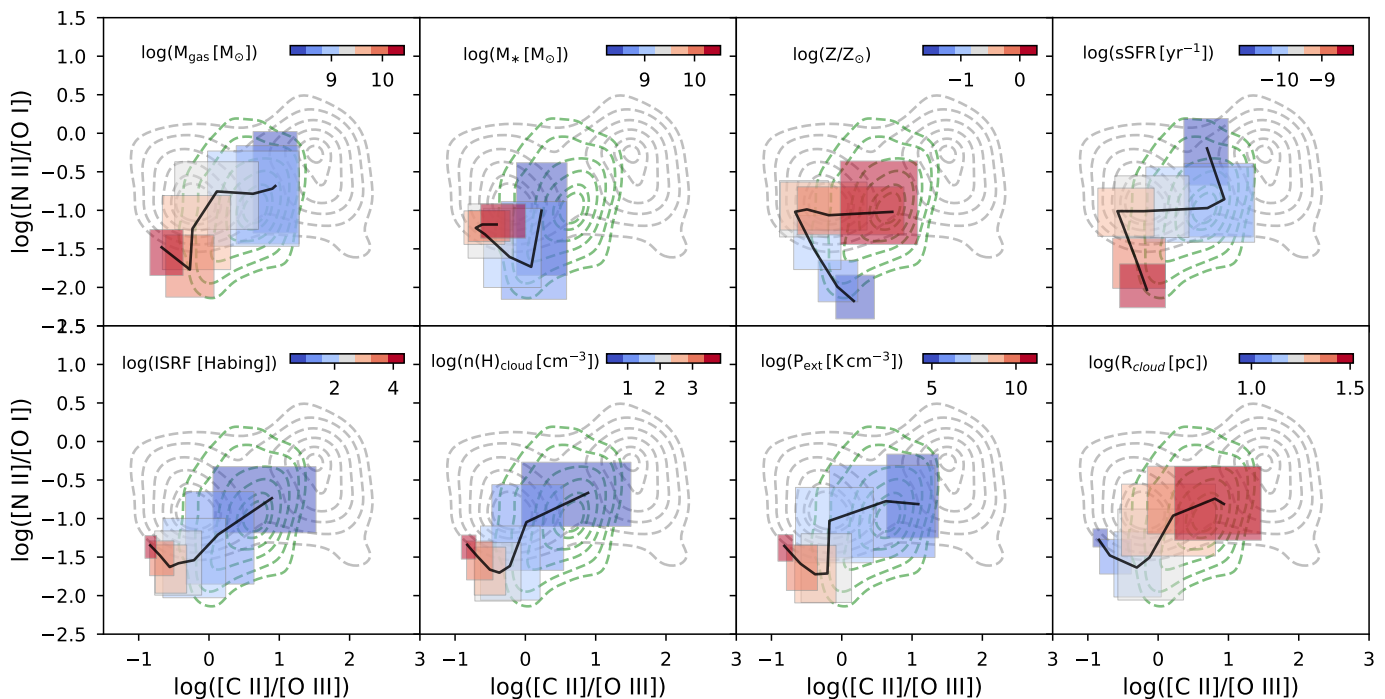


Fig. 18. Physical parameters in the diagnostic plot comparing the $[C II]/[O III]$ ratio against the $[N II]/[O I]$ ratio. Colour-codes are the same as in Fig. 17.

crease the luminosity by increasing this density and vice-versa. The use of different densities could be important when comparing the contributions of DIG and HII regions, especially in lines such as $[O III]$ and $[N III]$ (see Figs. 11 and 13). This DIG–HII region balance is still unclear in ionised emission lines, and although some estimates exist from optical wavelengths (e.g. Piotrodjojo et al. 2019), a change in this balance can lead to different metallicities, which may affect high- z studies (Sanders et al. 2017). In this work, we calibrate the DIG with observational data at $z = 0$, which may also bias the balance between these two ISM phases. Fortunately, the results presented in this work show that these assumptions seem to be in agreement with the observations, which may represent a likely first step in understanding the DIG–HII region balance.

Finally, our predictions depend on CLOUDY lookup tables, which can give different emissivities depending on the assumed initial abundances or dust configurations (Ploekinger & Schaye 2020). Different photoionisation models could lead to different interpretations of physical parameters coming from line ratios, such as metallicity or ionisation parameter (e.g. Ji & Yan 2022). Furthermore the intrinsic thermodynamics may not be the same in terms of cooling and heating functions in cosmological simulations and photoionisation models like CLOUDY (Robinson et al. 2021). Therefore, some care must be taken when interpreting the line luminosities predicted by our model.

5.2. The use of EAGLE

In this work we use the EAGLE simulation as a proxy of what we would expect to see in the Universe. However, by using a cosmological simulation like EAGLE, our line luminosity predictions of the ISM model are expected to inherit the limitations of the simulation. An example of these limitations is the lack of starburst-like galaxies within EAGLE (Wang et al. 2019b). As we discussed in Paper I, this restricts our comparison at $z = 0$

mainly to SFR below $10 M_{\odot} \text{ yr}^{-1}$ but also limits the comparisons at other redshifts (Katsianis et al. 2017). To compare our predictions with high SFR observations, we extrapolate the linear relations in the range of $-3.5 < \log(\text{SFR}) < 3.5$. However, care must be taken when using this extrapolation.

Another important physical property within EAGLE that affects our predictions is the gas metallicity, which is usually studied through the gas-phase mass–metallicity relation (MZR). Bellstedt et al. (2021) show that the MZR in EAGLE galaxies, as measured by Zenocratti et al. (2020) at $z = 0$, does not behave similarly to other cosmological simulations or semi-analytical models. As shown in Fig. 4 of Bellstedt et al. (2021), the metallicities in EAGLE have values around $12 + \log(O/H) \sim 9$ for stellar masses between $9 < \log(M_{*}[M_{\odot}]) < 11$, which is high compared to observations with metallicities going from $12 + \log(O/H) \sim 8.5$ to $12 + \log(O/H) \sim 9.2$ in the same stellar mass range. This may affect the metallicity that can be recovered from FIR lines if only $z = 0$ is used. However, MZR in EAGLE depends on resolution and box-size used due to the assumed AGN and star formation feedback processes (De Rossi et al. 2017). In Figs. 17 and 18, we present the predicted luminosities in different boxes and redshifts studied in this work and find that some of the FIR line ratios can be useful to infer the metallicity. Therefore, it will be important to compare the FIR line predictions that trace metallicity with observations in the future more consistently.

Although we base our predictions on EAGLE, we expect that similar physical models and/or cosmological simulations can be used to understand the gas properties with FIR emission lines. For example, Olsen et al. (2021) show that these kinds of predictions can be obtained with a different gas fragmentation scheme using SIGAME, which are similar to observations and our predictions. However, most of the galaxies in SIGAME have higher SFR than those studied in this work. This difference in the sample of simulated galaxies comes from choosing a different simulation (SIMBA instead of EAGLE), which allows for the forma-

tion of starburst-like systems. Therefore, although some physical assumptions are different for each model and are limited by the simulation used (e.g. Vallini et al. 2015; Lagache et al. 2018; Popping et al. 2019; Pallottini et al. 2019; Leung et al. 2020), we expect predictions to behave similarly to those presented in this work. In the future, we will compare results from different simulations, such as SIMBA and ILLUSTRISTNG in an efficient way to reduce the bias that the initial assumptions of the simulations may introduce.

5.3. Observational data from samples

For our comparison between observations and our model line luminosities, we have collected a heterogeneous sample of observed galaxies with FIR emission line information. We have transformed the luminosities of the lines to the same reference cosmology (Planck Collaboration et al. 2014) and we have estimated the SFR in most of the cases following the L_{IR} –SFR relation described by Kennicutt & Evans (2012). However, there are some other important issues that may affect this heterogeneous sample.

The most important issue may come from the initial mass function (IMF) assumed to estimate the SFRs. Unfortunately, IMF information is not always present in papers. Assuming a star-formation law that takes into account a standard IMF is a possible solution, as we have tried in this work. However, this may add additional uncertainties. For example, EAGLE uses an instantaneous SFR, which is different from the SFR averaged over the last 10 or 100 Myr typically used in observations. Another problem is that some of the SFR (or L_{IR}) may come from spectral energy distribution (SED) models rather than empirical laws using FIR photometric bands, like IRAS, PACS or SPIRE. In addition, the IR luminosity definition can have different flavours (e.g. L_{IR} , L_{FIR} or L_{TIR}) that use different wavelength ranges to estimate luminosities, adding to the spread of SFR estimates (Förster Schreiber & Wuyts 2020) and leading to differences of factors between 1.1 and 1.7 (De Looze et al. 2014; Lagache et al. 2018). Another possibility is to use other SFR tracers, such as H α -based, UV-based, or radio-based SFRs as shown in many studies (e.g. Wang et al. 2016, 2019a). However, in some cases, such as in high- z galaxies, it can be difficult to obtain such SFRs estimates and other lines like [C II] come into play as a SFR tracer (Le Fèvre et al. 2020), as we have also shown in this work.

In addition to theoretical considerations, some of the FIR line measurements have systematic uncertainties. For example, calibration pipelines or the use of different instruments may affect the comparison, as shown by Lamarche et al. (2018) in the case of H-ATLAS J091043.0-000322, discussed in Sect. 4.1. Furthermore, different-sized (or -shaped) apertures in the observational sample may affect the analysis of the fixed-size aperture we selected for the simulated galaxies (30 pkpc). For example, the balance between DIG and HII regions as main contributors to the ionised lines could depend on the selected aperture, as indicated by Mannucci et al. (2021). Finally, gravitational lensing can introduce a large uncertainty in the luminosities, which can be reduced by a factor of 30 to 40 in some galaxies when corrected by the magnification factor (e.g. in Eyelash and SPT-S J041839-4751.8, Zhang et al. 2018; Rizzo et al. 2020, respectively). In addition, these magnification factors may change depending on the observed region of the galaxy (Lamarche et al. 2018). In this work, we highlight those galaxies to warn about these potential complications, but in general, they show good agreement with our predictions.

6. Summary and Conclusions

We have modelled FIR emission lines by post-processing EAGLE cosmological simulations using CLOUDY. We have predicted the luminosities of the eight most important lines in the FIR up to $z = 6$, using a physically motivated model that traces four different ISM phases: dense molecular gas, neutral atomic gas, diffuse ionised gas and HII regions. We have also collected a sample of observed galaxies from the literature with which to compare with our predictions. Our main conclusions are as follows.

1. Predictions from our model replicate observed galaxies in the SFR–FIR line luminosity relationship to an average degree of 0.5 dex over the range $z = 0$ – 6 , which is reasonable considering the observational measurements errors. We also compare with different models showing similar level of agreement. We model the SFR–FIR line luminosity relationship for each of the eight lines with a linear relation, each of which shows a slight evolution with redshift.
2. We have presented the expected contributions of each ISM phase to each FIR line. These contributions change as a function of SFR. For the [C II] 158 μm line, the main contributor is the neutral atomic gas, with considerable contributions from HII regions at $z = 1$ – 4 and the DIG at $z < 2$, which may be related to metallicity. For the [N II] lines at 122 and 205 μm , the DIG contributes more than HII regions in the local Universe, but the opposite is true at high- z , where HII regions seem to dominate over the DIG. For the [O I] lines at 63 and 145 μm , the contribution of dense molecular gas is important in the local Universe. However, the atomic gas is dominant at high- z . Finally, for the [O III] lines at 52 and 88 μm and [N III] at 57 μm , we show that HII regions dominate, with important contribution from the DIG at low SFR in the local Universe.
3. Our predictions indicate that [C II] may not be a good SFR tracer for starburst galaxies, since the [C II]/SFR ratio seems to decrease as a function of the offset from the star-forming main-sequence. However, compared to the other FIR lines, [C II] seems to be the best SFR tracer due to its weak redshift evolution. [O III] and [O I] may also be good SFR tracers. Nonetheless, our predictions of [O III] at $z = 0$ may be underestimated, and more observations of [O I] are necessary at $z < 4$ to confirm our predictions.
4. We compare our predictions in two diagnostic diagrams, and we find reasonable agreement with observations. We compare $L_{[\text{O III}]}/\text{SFR}$ and $L_{[\text{C II}]}/\text{SFR}$ ratios and find that mock galaxies at high- z tend to have higher $L_{[\text{O III}]}/\text{SFR}$ ratios and slightly lower $L_{[\text{C II}]}/\text{SFR}$ ratios than galaxies in the local Universe. We also compare the [C II]/[O III] and [N II]/[O I] ratios and find that mock galaxies at high- z tend to have lower [C II]/[O III] and [N II]/[O I] ratios than galaxies in the local Universe.
5. Finally, we have examined the impact of physical parameters on these diagnostic diagrams. When we compare physical parameters to line luminosities, we find that $L_{[\text{C II}]}/\text{SFR}$ and $L_{[\text{O III}]}/\text{SFR}$ ratios trace hydrogen density and ISRF well in the mock galaxies. However, these ratios are not good metallicity tracers, because $L_{[\text{O III}]}/\text{SFR}$ does not evolve linearly with metallicity and $L_{[\text{C II}]}/\text{SFR}$ does not change with metallicity. Furthermore, we find that [C II]/[O III] and [N II]/[O I] ratios can be good metallicity and sSFR tracers. For example, [C II]/[O III] can trace metallicities close to solar and [N II]/[O I] below solar. On the other hand, we can identify systems with different sSFRs by means of both [C II]/[O III]

and $[N\text{ II}]/[O\text{ I}]$ ratios, which can be very useful for improving calibrations of $[C\text{ II}]$ as a SFR tracer.

In the future we expect to use this model and its predictions to understand the effect that AGN can have on the ISM, as well as the physical parameters traced by these lines and their ratios. We make our model predictions and collected observational sample publicly available to allow potential users to compare with their work and/or interpret new observations. We envisage that our predictions will also be useful in planning for future FIR missions.

Acknowledgements. The authors thank Karen Pardos Olsen for providing the data from the SIGAME framework. This research has made use of the 3Mdb database⁴ (Morisset et al. 2015) from which initial experiments to model H α regions were performed. This research made use of Astropy,⁵ a community-developed core Python package for Astronomy (Astropy Collaboration et al. 2013, 2018). This research made use of several Python packages, among them: numpy (Harris et al. 2020), pandas (Wes McKinney 2010) and matplotlib (Hunter 2007). This research has made use of the SIMBAD database, operated at CDS, Strasbourg, France. This research has made use of the NASA/IPAC Extragalactic Database (NED), which is funded by the National Aeronautics and Space Administration and operated by the California Institute of Technology. This research has made use of NASA's Astrophysics Data System Bibliographic Services. The EAGLE simulations were performed using the DiRAC-2 facility at Durham, managed by the ICC, and the PRACE facility Curie based in France at TGCC, CEA, Bruyères-le-Châtel. We would like to thank the Center for Information Technology of the University of Groningen for their support and for providing access to the Peregrine high performance computing cluster.

References

- Abdullah, A., Brandl, B. R., Groves, B., et al. 2017, *ApJ*, 842, 4
- Abdullah, A. & Tielens, A. G. G. M. 2020, *A&A*, 639, A110
- Arata, S., Yajima, H., Nagamine, K., Abe, M., & Khochfar, S. 2020, *MNRAS*, 498, 5541
- Aravena, M., Decarli, R., Walter, F., et al. 2016, *ApJ*, 833, 71
- Armus, L., Mazzarella, J. M., Evans, A. S., et al. 2009, *PASP*, 121, 559
- Ashby, M. L. N., Mahajan, S., Smith, H. A., et al. 2011, *PASP*, 123, 1011
- Astropy Collaboration, Price-Whelan, A. M., Sipőcz, B. M., et al. 2018, *AJ*, 156, 123
- Astropy Collaboration, Robitaille, T. P., Tollerud, E. J., et al. 2013, *A&A*, 558, A33
- Bellstedt, S., Robotham, A. S. G., Driver, S. P., et al. 2021, *MNRAS*, 503, 3309
- Béthermin, M., De Breuck, C., Gullberg, B., et al. 2016, *A&A*, 586, L7
- Béthermin, M., Fudamoto, Y., Ginolfi, M., et al. 2020, *A&A*, 643, A2
- Bordalo, V., Plana, H., & Telles, E. 2009, *ApJ*, 696, 1668
- Bouwens, R. J., Smit, R., Schouws, S., et al. 2021, arXiv e-prints, arXiv:2106.13719
- Brauher, J. R., Dale, D. A., & Helou, G. 2008, *ApJS*, 178, 280
- Brisbin, D., Ferkinhoff, C., Nikola, T., et al. 2015, *ApJ*, 799, 13
- Bussmann, R. S., Pérez-Fournon, I., Amber, S., et al. 2013, *ApJ*, 779, 25
- Camps, P. & Baes, M. 2020, *Astronomy and Computing*, 31, 100381
- Capak, P. L., Carilli, C., Jones, G., et al. 2015, *Nature*, 522, 455
- Carilli, C. L. & Walter, F. 2013, *ARA&A*, 51, 105
- Carniani, S., Ferrara, A., Maiolino, R., et al. 2020, *MNRAS*, 499, 5136
- Cheng, C., Cao, X., Lu, N., et al. 2020, *ApJ*, 898, 33
- Cigan, P., Young, L., Cormier, D., et al. 2016, *AJ*, 151, 14
- Cooray, A., Calanog, J., Wardlow, J. L., et al. 2014, *ApJ*, 790, 40
- Coppin, K. E. K., Danielson, A. L. R., Geach, J. E., et al. 2012, *MNRAS*, 427, 520
- Cormier, D., Abel, N. P., Hony, S., et al. 2019, *A&A*, 626, A23
- Cormier, D., Lebouteiller, V., Madden, S. C., et al. 2012, *A&A*, 548, A20
- Cormier, D., Madden, S. C., Lebouteiller, V., et al. 2015, *A&A*, 578, A53
- Cortés, J. R., Kenney, J. D. P., & Hardy, E. 2008, *ApJ*, 683, 78
- Crain, R. A., Schaye, J., Bower, R. G., et al. 2015, *MNRAS*, 450, 1937
- Croxall, K. V., Smith, J. D., Pellegrini, E., et al. 2017, *ApJ*, 845, 96
- Cunningham, D. J. M., Chapman, S. C., Aravena, M., et al. 2020, *MNRAS*, 494, 4090
- Dalla Vecchia, C. & Schaye, J. 2012, *MNRAS*, 426, 140
- Davé, R., Anglés-Alcázar, D., Narayanan, D., et al. 2019, *MNRAS*, 486, 2827
- Dayal, P. & Ferrara, A. 2018, *Phys. Rep.*, 780, 1
- De Breuck, C., Weiß, A., Béthermin, M., et al. 2019, *A&A*, 631, A167
- De Looze, I., Cormier, D., Lebouteiller, V., et al. 2014, *A&A*, 568, A62
- De Rossi, M. E., Bower, R. G., Font, A. S., Schaye, J., & Theuns, T. 2017, *MNRAS*, 472, 3354
- Decarli, R., Walter, F., Carilli, C., et al. 2014, *ApJ*, 782, L17
- Decarli, R., Walter, F., Neri, R., et al. 2012, *ApJ*, 752, 2
- Decarli, R., Walter, F., Venemans, B. P., et al. 2017, *Nature*, 545, 457
- Decataldo, D., Lupi, A., Ferrara, A., Pallottini, A., & Fumagalli, M. 2020, *MNRAS*, 497, 4718
- Deharveng, L., Schuller, F., Anderson, L. D., et al. 2010, *A&A*, 523, A6
- Dessauges-Zavadsky, M., Richard, J., Combes, F., et al. 2019, *Nature Astronomy*, 3, 1115
- Díaz-Santos, T., Armus, L., Charmandaris, V., et al. 2017, *ApJ*, 846, 32
- Dolag, K., Borgani, S., Murante, G., & Springel, V. 2009, *MNRAS*, 399, 497
- Draine, B. T. 2011, *Physics of the Interstellar and Intergalactic Medium*
- Duarte Puertas, S., Vilchez, J. M., Iglesias-Páramo, J., et al. 2017, *A&A*, 599, A71
- Evans, A. S., Solomon, P. M., Tacconi, L. J., Vavilkin, T., & Downes, D. 2006, *AJ*, 132, 2398
- Faisst, A. L., Capak, P. L., Yan, L., et al. 2017, *ApJ*, 847, 21
- Farrah, D., Lebouteiller, V., Spoon, H. W. W., et al. 2013, *ApJ*, 776, 38
- Ferkinhoff, C., Brisbin, D., Nikola, T., et al. 2011, *ApJ*, 740, L29
- Ferkinhoff, C., Brisbin, D., Nikola, T., et al. 2015, *ApJ*, 806, 260
- Ferkinhoff, C., Hailey-Dunsheath, S., Nikola, T., et al. 2010, *ApJ*, 714, L147
- Ferland, G. J. 1996, *Hazy, A Brief Introduction to Cloudy 90*
- Ferland, G. J., Chatzikos, M., Guzmán, F., et al. 2017, *Rev. Mexicana Astron. Astrofis.*, 53, 385
- Fernández-Ontiveros, J. A., Pérez-Montero, E., Vílchez, J. M., Amorín, R., & Spinoglio, L. 2021, *A&A*, 652, A23
- Fernández-Ontiveros, J. A., Spinoglio, L., Pereira-Santaella, M., et al. 2016, *ApJS*, 226, 19
- Ferrara, A., Vallini, L., Pallottini, A., et al. 2019, *MNRAS*, 489, 1
- Förster Schreiber, N. M. & Wuyts, S. 2020, *ARA&A*, 58, 661

⁴ <https://sites.google.com/site/mexicanmillionmodels>

⁵ <http://www.astropy.org>

- Fraser-McKelvie, A., Brown, M. J. I., & Pimblett, K. A. 2014, *MNRAS*, 444, L63
- Fraternali, F., Karim, A., Magnelli, B., et al. 2021, *A&A*, 647, A194
- Fujimoto, S., Oguri, M., Brammer, G., et al. 2021, *ApJ*, 911, 99
- Furlong, M., Bower, R. G., Theuns, T., et al. 2015, *MNRAS*, 450, 4486
- Gavazzi, G., Boselli, A., Scodreggio, M., Pierini, D., & Belsole, E. 1999, *MNRAS*, 304, 595
- Gavazzi, R., Cooray, A., Conley, A., et al. 2011, *ApJ*, 738, 125
- Goldsmith, P. F. 2019, *ApJ*, 887, 54
- Goldsmith, P. F., Langer, W. D., Pineda, J. L., & Velusamy, T. 2012, *ApJS*, 203, 13
- Goldsmith, P. F., Yıldız, U. A., Langer, W. D., & Pineda, J. L. 2015, *ApJ*, 814, 133
- Gong, Y., Cooray, A., Silva, M., et al. 2012, *ApJ*, 745, 49
- Greve, T. R., Vieira, J. D., Weiß, A., et al. 2012, *ApJ*, 756, 101
- Gullberg, B., De Breuck, C., Vieira, J. D., et al. 2015, *MNRAS*, 449, 2883
- Gullberg, B., Swinbank, A. M., Smail, I., et al. 2018, *ApJ*, 859, 12
- Haffner, L. M., Dettmar, R. J., Beckman, J. E., et al. 2009, *Reviews of Modern Physics*, 81, 969
- Harikane, Y., Ouchi, M., Inoue, A. K., et al. 2020, *ApJ*, 896, 93
- Harrington, K. C., Vishwas, A., Weiß, A., et al. 2019, *MNRAS*, 488, 1489
- Harris, C. R., Millman, K. J., van der Walt, S. J., et al. 2020, *Nature*, 585, 357
- Hashimoto, T., Inoue, A. K., Tamura, Y., et al. 2019, *PASJ*, 71, 109
- Herrera-Camus, R., Bolatto, A., Smith, J. D., et al. 2016, *ApJ*, 826, 175
- Herrera-Camus, R., Bolatto, A. D., Wolfire, M. G., et al. 2015, *ApJ*, 800, 1
- Herrera-Camus, R., Sturm, E., Graciá-Carpio, J., et al. 2018a, *ApJ*, 861, 94
- Herrera-Camus, R., Sturm, E., Graciá-Carpio, J., et al. 2018b, *ApJ*, 861, 95
- Hodge, J. A. & da Cunha, E. 2020, *Royal Society Open Science*, 7, 200556
- Hopkins, P. F. 2013, *MNRAS*, 428, 2840
- Hunter, J. D. 2007, *Computing in Science & Engineering*, 9, 90
- Inoue, A. K., Shimizu, I., Tamura, Y., et al. 2014, *ApJ*, 780, L18
- Inoue, A. K., Tamura, Y., Matsuo, H., et al. 2016, *Science*, 352, 1559
- Inoue, S., Matsuo, H., Yoshida, N., Yajima, H., & Moriwaki, K. 2021, *arXiv e-prints*, arXiv:2102.10752
- Iono, D., Yun, M. S., Elvis, M., et al. 2006, *ApJ*, 645, L97
- Ji, X. & Yan, R. 2022, *A&A*, 659, A112
- Kamenetzky, J., Rangwala, N., Glenn, J., Maloney, P. R., & Conley, A. 2016, *ApJ*, 829, 93
- Kannan, R., Smith, A., Garaldi, E., et al. 2021, *arXiv e-prints*, arXiv:2111.02411
- Karachentsev, I. D. & Makarov, D. A. 1996, *AJ*, 111, 794
- Karachentsev, I. D., Tully, R. B., Wu, P.-F., Shaya, E. J., & Dolphin, A. E. 2014, *ApJ*, 782, 4
- Katsianis, A., Blanc, G., Lagos, C. P., et al. 2017, *MNRAS*, 472, 919
- Katz, H., Galligan, T. P., Kimm, T., et al. 2019, *MNRAS*, 487, 5902
- Katz, H., Rosdahl, J., Kimm, T., et al. 2022, *MNRAS*, 510, 5603
- Kennicutt, R. C. & Evans, N. J. 2012, *ARA&A*, 50, 531
- Kewley, L. J., Nicholls, D. C., & Sutherland, R. S. 2019, *ARA&A*, 57, 511
- Khan-Ali, A., Carrera, F. J., Page, M. J., et al. 2015, *MNRAS*, 448, 75
- Knudsen, K. K., Richard, J., Kneib, J.-P., et al. 2016, *MNRAS*, 462, L6
- Komatsu, E., Dunkley, J., Nolta, M. R., et al. 2009, *ApJS*, 180, 330
- Kramida, A., Yu. Ralchenko, Reader, J., & and NIST ASD Team. 2020, *NIST Atomic Spectra Database (ver. 5.8)*, [Online]. Available: <https://physics.nist.gov/asd> [2021, July 23]. National Institute of Standards and Technology, Gaithersburg, MD.
- Kurtz, S. 2005, in *Massive Star Birth: A Crossroads of Astrophysics*, ed. R. Cesaroni, M. Felli, E. Churchwell, & M. Walmsley, Vol. 227, 111–119
- Lagache, G., Cousin, M., & Chatzikos, M. 2018, *A&A*, 609, A130
- Lamarche, C., Verma, A., Vishwas, A., et al. 2018, *ApJ*, 867, 140
- Langer, W. D., Pineda, J. L., Goldsmith, P. F., et al. 2021, *A&A*, 651, A59
- Le Fèvre, O., Béthermin, M., Faisst, A., et al. 2020, *A&A*, 643, A1
- Lee, M. M., Nagao, T., De Breuck, C., et al. 2019, *ApJ*, 883, L29
- Lee, M. M., Nagao, T., De Breuck, C., et al. 2021, *ApJ*, 913, 41
- Leitherer, C., Ekström, S., Meynet, G., et al. 2014, *ApJS*, 212, 14
- Lestrade, J.-F., Carilli, C. L., Thanjavur, K., et al. 2011, *ApJ*, 739, L30
- Leung, T. K. D., Olsen, K. P., Somerville, R. S., et al. 2020, *ApJ*, 905, 102
- Li, J., Wang, R., Cox, P., et al. 2020, *ApJ*, 900, 131
- Madau, P. & Dickinson, M. 2014, *ARA&A*, 52, 415
- Magdis, G. E., Rigopoulou, D., Hopwood, R., et al. 2014, *ApJ*, 796, 63
- Maiolino, R., Cox, P., Caselli, P., et al. 2005, *A&A*, 440, L51
- Malhotra, S., Kaufman, M. J., Hollenbach, D., et al. 2001, *ApJ*, 561, 766
- Mannucci, F., Belfiore, F., Curti, M., et al. 2021, *MNRAS*, 508, 1582
- Matthee, J., Sobral, D., Boogaard, L. A., et al. 2019, *ApJ*, 881, 124
- McAlpine, S., Helly, J. C., Schaller, M., et al. 2016, *Astronomy and Computing*, 15, 72
- Mitsunashi, I., Matsuda, Y., Smail, I., et al. 2021, *ApJ*, 907, 122
- Mordini, S., Spinoglio, L., & Fernández-Ontiveros, J. A. 2021, *A&A*, 653, A36
- Morisset, C., Delgado-Inglada, G., & Flores-Fajardo, N. 2015, *Rev. Mexicana Astron. Astrofis.*, 51, 103
- Moriwaki, K., Yoshida, N., Shimizu, I., et al. 2018, *MNRAS*, 481, L84
- Nagao, T., Maiolino, R., Marconi, A., & Matsuhara, H. 2011, *A&A*, 526, A149
- Neeleman, M., Bañados, E., Walter, F., et al. 2019, *ApJ*, 882, 10
- Neeleman, M., Prochaska, J. X., Kanekar, N., & Rafelski, M. 2020, *Nature*, 581, 269
- Olivares E., F., Hamuy, M., Pignata, G., et al. 2010, *ApJ*, 715, 833
- Olsen, K., Greve, T. R., Narayanan, D., et al. 2017, *ApJ*, 846, 105
- Olsen, K., Greve, T. R., Narayanan, D., et al. 2018, *ApJ*, 857, 148
- Olsen, K. P., Burkhart, B., Mac Low, M.-M., et al. 2021, *ApJ*, 922, 88
- Olsen, K. P., Greve, T. R., Narayanan, D., et al. 2015, *ApJ*, 814, 76

- Oteo, I., Ivison, R. J., Dunne, L., et al. 2016, *ApJ*, 827, 34
- Pallottini, A., Ferrara, A., Decataldo, D., et al. 2019, *MNRAS*, 487, 1689
- Pallottini, A., Ferrara, A., Gallerani, S., et al. 2022, arXiv e-prints, arXiv:2201.02636
- Pavesi, R., Riechers, D. A., Capak, P. L., et al. 2016, *ApJ*, 832, 151
- Peñaloza, C. H., Clark, P. C., Glover, S. C. O., & Klessen, R. S. 2018, *MNRAS*, 475, 1508
- Pineda, J. L., Fischer, C., Kapala, M., et al. 2018, *ApJ*, 869, L30
- Planck Collaboration, Ade, P. A. R., Aghanim, N., et al. 2014, *A&A*, 571, A16
- Ploeckinger, S. & Schaye, J. 2020, *MNRAS*, 497, 4857
- Podigachoski, P., Barthel, P. D., Haas, M., et al. 2015, *A&A*, 575, A80
- Poetrodjojo, H., D’Agostino, J. J., Groves, B., et al. 2019, *MNRAS*, 487, 79
- Pokhrel, N. R., Simpson, C. E., & Bagetakos, I. 2020, *AJ*, 160, 66
- Popping, G., Narayanan, D., Somerville, R. S., Faisst, A. L., & Krumholz, M. R. 2019, *MNRAS*, 482, 4906
- Rahmati, A., Pawlik, A. H., Raičević, M., & Schaye, J. 2013, *MNRAS*, 430, 2427
- Ramos Padilla, A. F., Wang, L., Małek, K., Efstathiou, A., & Yang, G. 2022, *MNRAS*, 510, 687
- Ramos Padilla, A. F., Wang, L., Ploeckinger, S., van der Tak, F. F. S., & Trager, S. C. 2021, *A&A*, 645, A133
- Rémy-Ruyer, A., Madden, S. C., Galliano, F., et al. 2013, *A&A*, 557, A95
- Rigopoulou, D., Pereira-Santaella, M., Magdis, G. E., et al. 2018, *MNRAS*, 473, 20
- Rizzo, F., Vegetti, S., Fraternali, F., Stacey, H. R., & Powell, D. 2021, *MNRAS*, 507, 3952
- Rizzo, F., Vegetti, S., Powell, D., et al. 2020, *Nature*, 584, 201
- Robinson, D., Avestruz, C., & Gnedin, N. Y. 2021, arXiv e-prints, arXiv:2109.01674
- Rodríguez, Ó., Clocchiatti, A., & Hamuy, M. 2014, *AJ*, 148, 107
- Rosas-Guevara, Y. M., Bower, R. G., Schaye, J., et al. 2015, *MNRAS*, 454, 1038
- Rosenberg, M. J. F., van der Werf, P. P., Aalto, S., et al. 2015, *ApJ*, 801, 72
- Ruiz, A., Risaliti, G., Nardini, E., Panessa, F., & Carrera, F. J. 2013, *A&A*, 549, A125
- Rybak, M., da Cunha, E., Groves, B., et al. 2021, *ApJ*, 909, 130
- Rybak, M., Zavala, J. A., Hodge, J. A., Casey, C. M., & Werf, P. v. d. 2020, *ApJ*, 889, L11
- Sanders, R. L., Shapley, A. E., Zhang, K., & Yan, R. 2017, *ApJ*, 850, 136
- Saturni, F. G., Trevese, D., Vagnetti, F., Perna, M., & Dadina, M. 2016, *A&A*, 587, A43
- Schaerer, D., Ginolfi, M., Béthermin, M., et al. 2020, *A&A*, 643, A3
- Schaller, G., Schaerer, D., Meynet, G., & Maeder, A. 1992, *A&AS*, 96, 269
- Schaye, J., Crain, R. A., Bower, R. G., et al. 2015, *MNRAS*, 446, 521
- Schaye, J. & Dalla Vecchia, C. 2008, *MNRAS*, 383, 1210
- Shi, Y., Rieke, G. H., Ogle, P. M., Su, K. Y. L., & Balog, Z. 2014, *ApJS*, 214, 23
- Smith, B. J., Wagstaff, P., Struck, C., et al. 2019, *AJ*, 158, 169
- Speagle, J. S., Steinhardt, C. L., Capak, P. L., & Silverman, J. D. 2014, *ApJS*, 214, 15
- Spergel, D. N., Verde, L., Peiris, H. V., et al. 2003, *ApJS*, 148, 175
- Spilker, J. S., Marrone, D. P., Aravena, M., et al. 2016, *ApJ*, 826, 112
- Spilker, J. S., Phadke, K. A., Aravena, M., et al. 2020, *ApJ*, 905, 85
- Spinoglio, L., Alonso-Herrero, A., Armus, L., et al. 2017, *PASA*, 34, e057
- Spinoglio, L., Pereira-Santaella, M., Dasyra, K. M., et al. 2015, *ApJ*, 799, 21
- Springel, V. 2005, *MNRAS*, 364, 1105
- Springel, V., Di Matteo, T., & Hernquist, L. 2005, *MNRAS*, 361, 776
- Springel, V., White, S. D. M., Tormen, G., & Kauffmann, G. 2001, *MNRAS*, 328, 726
- Stacey, G. J., Geis, N., Genzel, R., et al. 1991, *ApJ*, 373, 423
- Stacey, G. J., Hailey-Dunsheath, S., Ferkinhoff, C., et al. 2010, *ApJ*, 724, 957
- Stacey, H. R., McKean, J. P., Powell, D. M., et al. 2021, *MNRAS*, 500, 3667
- Sun, G., Hensley, B. S., Chang, T.-C., Doré, O., & Serra, P. 2019, *ApJ*, 887, 142
- Swinbank, A. M., Karim, A., Smail, I., et al. 2012, *MNRAS*, 427, 1066
- Tadaki, K.-i., Iono, D., Hatsukade, B., et al. 2019, *ApJ*, 876, 1
- Tarantino, E., Bolatto, A. D., Herrera-Camus, R., et al. 2021, *ApJ*, 915, 92
- Tateuchi, K., Konishi, M., Motohara, K., et al. 2015, *ApJS*, 217, 1
- Tayal, S. S. 2011, *ApJS*, 195, 12
- The EAGLE team. 2017, arXiv e-prints, arXiv:1706.09899
- Tielens, A. G. G. M. & Hollenbach, D. 1985, *ApJ*, 291, 722
- Tully, R. B., Courtois, H. M., Dolphin, A. E., et al. 2013, *AJ*, 146, 86
- Uzgil, B. D., Bradford, C. M., Hailey-Dunsheath, S., Maloney, P. R., & Aguirre, J. E. 2016, *ApJ*, 832, 209
- Vaddi, S., O’Dea, C. P., Baum, S. A., et al. 2016, *ApJ*, 818, 182
- Vallini, L., Ferrara, A., Pallottini, A., Carniani, S., & Gallerani, S. 2021, *MNRAS*, 505, 5543
- Vallini, L., Gallerani, S., Ferrara, A., & Baek, S. 2013, *MNRAS*, 433, 1567
- Vallini, L., Gallerani, S., Ferrara, A., Pallottini, A., & Yue, B. 2015, *ApJ*, 813, 36
- Valtchanov, I., Virdee, J., Ivison, R. J., et al. 2011, *MNRAS*, 415, 3473
- Vayner, A., Wright, S. A., Murray, N., et al. 2021, *ApJ*, 910, 44
- Venemans, B. P., Walter, F., Neeleman, M., et al. 2020, *ApJ*, 904, 130
- Vishwas, A., Ferkinhoff, C., Nikola, T., et al. 2018, *ApJ*, 856, 174
- Walter, F., Riechers, D., Novak, M., et al. 2018, *ApJ*, 869, L22
- Wang, L., Gao, F., Duncan, K. J., et al. 2019a, *A&A*, 631, A109
- Wang, L., Norberg, P., Gunawardhana, M. L. P., et al. 2016, *MNRAS*, 461, 1898
- Wang, L., Pearson, W. J., Cowley, W., et al. 2019b, *A&A*, 624, A98
- Wardlow, J. L., Cooray, A., Osage, W., et al. 2017, *ApJ*, 837, 12
- Wes McKinney. 2010, in *Proceedings of the 9th Python in Science Conference*, ed. Stéfan van der Walt & Jarrod Millman, 56 – 61
- Westhues, C., Haas, M., Barthel, P., et al. 2016, *AJ*, 151, 120
- Wiersma, R. P. C., Schaye, J., & Smith, B. D. 2009a, *MNRAS*, 393, 99
- Wiersma, R. P. C., Schaye, J., Theuns, T., Dalla Vecchia, C., & Tornatore, L. 2009b, *MNRAS*, 399, 574
- Wolfire, M. G., Vallini, L., & Chevance, M. 2022, arXiv e-prints, arXiv:2202.05867

- Yang, S. & Lidz, A. 2020, *MNRAS*, 499, 3417
- Yang, S., Lidz, A., & Popping, G. 2021a, *MNRAS*, 504, 723
- Yang, S., Popping, G., Somerville, R. S., et al. 2022, *ApJ*, 929, 140
- Yang, S., Somerville, R. S., Pullen, A. R., et al. 2021b, *ApJ*, 911, 132
- Zanella, A., Daddi, E., Magdis, G., et al. 2018, *MNRAS*, 481, 1976
- Zenocratti, L. J., De Rossi, M. E., Lara-López, M. A., & Theuns, T. 2020, *MNRAS*, 496, L33
- Zhang, Z.-Y., Ivison, R. J., George, R. D., et al. 2018, *MNRAS*, 481, 59
- Zhao, Y., Lu, N., Xu, C. K., et al. 2016a, *ApJ*, 819, 69
- Zhao, Y., Yan, L., & Tsai, C.-W. 2016b, *ApJ*, 824, 146

Appendix A: Observational sample

We have collected measurements from the literature of the FIR emission lines predicted in this work. The observational sample is a heterogeneous selection of galaxies that covers the redshift range between 0 and 6.5. We present references of the works used in this sample of galaxies together with the number of measurements available per line in Table A.1. When possible we recalculated the luminosities and SFRs onto the Λ CDM cosmology used in this work (Planck Collaboration et al. 2014). When the cosmology is not explicitly mentioned, we assume it is the same as used in this work, so no corrections are applied. We flag those measurements where a magnification factor is involved in estimating a luminosity due to gravitational lensing. We estimate SFR in most of the literature samples from the infrared luminosity (L_{IR}) using the relation of Kennicutt & Evans (2012), which assumes a similar IMF (Kroupa) to the one used in EAGLE (Chabrier). Unless stated otherwise, we use the same infrared luminosities as published in the respective works. In cases where L_{IR} is unavailable or is unreliable due to measurement error, we use SFR estimates from other works. Additionally, we remove strong AGN galaxies (i.e. QSO and Blazar). This observational sample is available as a supplementary material in a Zenodo repository, at <https://doi.org/10.5281/zenodo.6576202>.

We now comment on some references for which special attention is needed.

Brauher et al. (2008): We use the median line flux in galaxies with more than one measurement. L_{IR} is calculated using the IRAS 60 and 100 μm fluxes as described in Brauher et al. (2008). For two galaxies (3C 368 and Z 25-7), we adopt the preferred Local Group velocity in NED to estimate the distance to these galaxies (Karachentsev & Makarov 1996). For 19 galaxies (DDO 50, IC 10, IC 1613, IC 342, M 33, M 81, M 82, Maffei 2, NGC 0185, NGC 0247, NGC 0300, NGC 1569, NGC 4236, NGC 4569, NGC 6503, NGC 6822, NGC 6946, VCC 1043 and VCC 92), we use the redshift-independent distances⁶ from NED (Gavazzi et al. 1999; Olivares E. et al. 2010; Tully et al. 2013; Karachentsev et al. 2014). Finally for 3C 368, we use the SFR from Podigachoski et al. (2015), and for NGC 4038 and NGC 4039, we use the SFRs from Herrera-Camus et al. (2018a).

Stacey et al. (2010): We adopt magnification factors of two and eight for SMM J22471-0206 and Hbootes03, respectively. Due to the uncertain magnification in all other galaxies, we flag their luminosities as a precaution. For five galaxies (2XMM J094144.6+385440, 3C 065, 3C 368, IRAS F10026+4949 and IRAS F22231-0512), we adopt the SFRs from other works (De Looze et al. 2014; Podigachoski et al. 2015; Khan-Ali et al. 2015; Vayner et al. 2021).

Decarli et al. (2012): We use updated values for the magnification factors: for QSO J0831+5245 we adopt the upper limit of eight (Saturni et al. 2016), and for [LWB2009]MM184222+593828 we adopt a value of 12 (Lestrade et al. 2011).

⁶ These distances come from methods that use standard candles or rules, such as Cepheids and globular clusters.

Farrah et al. (2013): We adopt the SFR value from Kamenetzky et al. (2016) for IRAS 00397-1312.

De Looze et al. (2014): We use the magnification factors of other works in cases where the lensing models are better, or for consistency with other references used in this work, for the following galaxies: SDP 81 (Valtchanov et al. 2011), QSO J0831+5245 (Saturni et al. 2016) and [CRR2012] HLS J091828.6+514223 (Lagache et al. 2018). In addition, we take the magnification factor and SFR for G15.v2.779, HFLS3 and SMM J22471-0206 from Cheng et al. (2020), Cooray et al. (2014) and Ferkinhoff et al. (2015), respectively. For the following galaxies, we take SFR values from the literature: 2XMM J094144.6+385440 (Khan-Ali et al. 2015), 3C 065 (Podigachoski et al. 2015), 3C 368 (Podigachoski et al. 2015), 3C 446 (Vayner et al. 2021), IRAS F22231-0512 (Vayner et al. 2021), SMM J02399-0136 (Ferkinhoff et al. 2015), IRAS F10026+4949 (Ruiz et al. 2013) and SWIRE J104704.97+592332.3 (Stacey et al. 2010).

Magdis et al. (2014): For HXMM01, we adopt the magnification factor from Wardlow et al. (2017). For HLock01, we adopt the magnification factor from Gavazzi et al. (2011).

Brisbin et al. (2015): We assume that the cosmology used is the one from Spergel et al. (2003), as they mention that their work is a continuation of Stacey et al. (2010). We assume that all galaxies in this sample are magnified (Zanella et al. 2018).

Spinoglio et al. (2015): L_{IR} is calculated with the IRAS 60 and 100 μm fluxes as described in Brauher et al. (2008).

Rosenberg et al. (2015): We use the redshift from NED and the infrared flux reported in their tables to estimate L_{IR} .

Ferkinhoff et al. (2015): Data for QSO J0831+5245 comes from Ferkinhoff et al. (2010), where we have adopted the magnification factor from Saturni et al. (2016). Although this galaxy is part of the sample, we do not use it for the comparison in this work because the SFR estimated from the L_{IR} is unreliable due to the contribution of the AGN. Reported luminosities for [N II] come from ZEUS for QSO J0831+5245 and SMM J02399-0136, and ALMA for Cloverleaf (QSO J1415+1129).

Gullberg et al. (2015): We take the magnification values from Spilker et al. (2016); we flag those as limits when there is no magnification factor available (e.g. for SPT-SJ051258-5935.6). For SPT-SJ055138-5057.9 we adopt the magnification factor from Cunningham et al. (2020), while for SPT-SJ053816-5030.8 we adopt the magnification factor (18.8) reported by Spilker et al. (2016).

Cigan et al. (2016): L_{IR} is calculated using the IRAS 60 and 100 μm fluxes as described in Brauher et al. (2008). For DDO 155 we use the estimated SFR from $H\alpha$ by Pokhrel et al. (2020).

Zhao et al. (2016a): We obtain redshifts from NED when available. For five galaxies (M82, NGC 1569, NGC 2976, NGC 3077 and NGC 4569) we use the redshift-independent distances from NED (Tully et al. 2013; Karachentsev et al. 2014). For NGC 3557 we use the preferred redshift distance. Most of the galaxies in this sample do not have an estimated SFR, so we use the SFRs from Brauher et al. (2008) and Díaz-Santos et al. (2017) for most of the missing estimates. We use SFRs from Kamenetzky et al. (2016) for UGC 2369 and NGC 5010, and Tateuchi et al. (2015) for IC 4518A.

Zhao et al. (2016b): Some of the galaxies are identified to have second velocity components in their spectra; therefore we use the median luminosity value in those cases.

Oteo et al. (2016): The pair of galaxies in this reference is treated as one galaxy (H-ATLAS J000307.2-330250), as the second component does not exist in SIMBAD. We use the IR luminosities derived from SED fitting from Stacey et al. (2021).

Kamenetzky et al. (2016): We assume that the additional regions in NGC 6946 and NGC 4038 (Antennae) are also part of the galaxy. We use SFRs from other references for the following galaxies: 3C 405 (Brauher et al. 2008); Mrk 1298 (Shi et al. 2014); IC 4518A (Tateuchi et al. 2015); 3C 315 and 3C 433 (Westhues et al. 2016); ESO 255-IG007, NGC 2976 and VV 705 (Zhao et al. 2016a); 3C 305 (Fernández-Ontiveros et al. 2016); 3C 31 (Vaddi et al. 2016); IRAS 08355-4944, IRAS F01417+1651, MCG-03-34-064, NGC 877 and VV340a (Díaz-Santos et al. 2017); and, Antennae and NGC 4151 (Herrera-Camus et al. 2018a).

Uzgil et al. (2016): We assume a magnification factor of 30 for IRAS F10214+4724. When correcting the L_{IR} for this magnification factor, the SFR derived from the Kennicutt & Evans (2012) relation is similar to the SFR estimated by Evans et al. (2006). We use the magnification factor of eight as an upper limit for QSO J0831+5245 (Saturni et al. 2016). We assume this work uses the cosmology of Komatsu et al. (2009).

Fernández-Ontiveros et al. (2016): L_{IR} is calculated with the IRAS 60 and 100 μm fluxes as described in Brauher et al. (2008). For LEDA 101275 and Mrk 463E we use the IR luminosity reported by Ashby et al. (2011). For eight galaxies (M82, NGC 1569, NGC 2976, NGC 3077 and NGC 4569) we use redshift-independent distances from NED (Tully et al. 2013). For NGC 4569 and NGC 6946 we adopt distances reported by Cortés et al. (2008) and Rodríguez et al. (2014), respectively. We use SFRs from other references for the following galaxies: 3C 405 (Brauher et al. 2008); IC 4518A (Tateuchi et al. 2015); 2E 4728, 3C 317 and MCG+05-33-005 (Fraser-McKelvie et al. 2014); 3C 33, 3C 234, 3C 315 and 3C 433 (Westhues et al. 2016); LEDA 3098117, LEDA 4666674, NGC 7592W and Z 468-2 (Díaz-Santos et al. 2017); Centaurus A and Circinus galaxy (Herrera-Camus et al. 2018a); Mrk 266B Smith et al. (2019); and, ESO 141-55, 2MASX J00535615-7038045, IRAS 03450+0055 and UGC 12138 Ramos Padilla et al. (2022).

Knudsen et al. (2016): We use only the information of [ZFM2015] A383 5.1, as observations of the other galaxy (MS0451-H) are only upper limits and are not identified as a galaxy in SIMBAD.

Díaz-Santos et al. (2017): Redshifts are taken from NED to convert from the WMAP cosmology (Komatsu et al. 2009) used for the sample in Armus et al. (2009) to the Planck cosmology used in this work. We obtain IR luminosities from the sample webpage⁷.

Olsen et al. (2017): We remove two galaxies that are not identified in SIMBAD (MS0451-H and [CFP2010]BDF 3299 sub-region).

Lagache et al. (2018): For some galaxies we use a different magnification factor to those reported in Lagache et al. (2018). For H-ATLAS J142413.9+022304 and SPT-S J034510-4725.6 we use the magnification factor used by Cheng et al. (2020), and for [CLM2003] J022802.97-041618.3 we use the values by Olsen et al. (2017). We use the IR luminosity value for AzTEC 3 from Stacey et al. (2021). For galaxies coming from Aravena et al. (2016) we use the IR luminosities of Faisst et al. (2017). We use the reported SFR instead of converting from the IR luminosities for [CLM2003] J022802.97-041618.3 and [WMH2013] 5. Finally, we use the SFR from Neeleman et al. (2020) for ALMA J081740.86+135138.2.

Vishwas et al. (2018): We use a magnification factor of seven so the dust disk of H-ATLAS J113526.3-014605 can be consistent with other high- z SMG.

Gullberg et al. (2018): The data presented with this reference is an improvement of the results presented in Swinbank et al. (2012).

Lamarque et al. (2018): We adopt the IR luminosity from Bussmann et al. (2013). Two velocity components are measured in the [C II] line of SPD 11. We adopt the magnification factor estimated for the dominant (red) component.

Rigopoulou et al. (2018): We adopt a magnification factor of 10.9 according to Gavazzi et al. (2011).

Zhang et al. (2018): We use the magnification factor reported in their Table 4. For H-ATLAS J084933.4+021443 and SDP 81, we adopt 2.8 and 25, respectively, as magnification factors (Wardlow et al. 2017; Valtchanov et al. 2011).

Cormier et al. (2019): We use distances reported by Rémy-Ruyer et al. (2013) in most of the galaxies. For ten galaxies (ESO 495-21, Mrk 209, NGC 1140, NGC 1569, NGC 1705, NGC 4214, NGC 5253, NGC 625, UGC 4483 and UGC 6456) we use redshift-independent distances from NED (Tully et al. 2013). For ESO 350-38 and HS 0822+3542 we use the preferred redshift values from NED. For UGCA 116 we use the

⁷ GOALS sample at <https://goals.ipac.caltech.edu>

distance reported in [Bordalo et al. \(2009\)](#). We use the reported distance used in [Cormier et al. \(2019\)](#) for Mrk 33 and discard the information from the LMC and SMC. For 2MASX J12390403+3920437 we use the SFR reported by [Duarte Puertas et al. \(2017\)](#).

[De Breuck et al. \(2019\)](#): We use the magnification factor of 32.7 by [Spilker et al. \(2016\)](#).

[Tadaki et al. \(2019\)](#): We assume the cosmology used is a Λ CDM cosmology with $\Omega = 0.27$ and $H_0 = 70 \text{ km s}^{-1} \text{ Mpc}^{-1}$.

[Neeleman et al. \(2019\)](#): For [NBW2019]J0842+1218C2 we assume that the upper limit for SFR is $100 M_{\odot} \text{ yr}^{-1}$.

[Lee et al. \(2019\)](#): We use the IR luminosity values and [C II] measurements from [Iono et al. \(2006\)](#).

[Hashimoto et al. \(2019\)](#): The reported values for the SFR are assumed to be upper limits, as those come from QSOs.

[B  thermin et al. \(2020\)](#): These objects have not been ingested in SIMBAD, but we use the coordinates of the closest object. However, this can lead to incorrect identifications. For example, the closest object to the coordinates of VUDS-COSMOS-5100541407 is a star (COSMOS 877137). Caution is therefore required. We use SFRs from SED fitting except for cases where it seems to be overestimated. For COSMOS-DEIMOS-873756 and VUDS-COSMOS-510596653 we assume the SFRs are upper limits, where for VUDS-COSMOS-510596653 we use the estimated IR luminosity and convert it to SFR.

[Venemans et al. \(2020\)](#): We do not include the companions of the galaxies, as those are not yet identified in SIMBAD.

[Cunningham et al. \(2020\)](#): We use the SFRs from [Gullberg et al. \(2015\)](#) for most of the galaxies. We obtain IR luminosities for SPT-S J234942-5638.2, SPT-S J235339-5010.1 and SPT-S J235718-5153.7 from [Greve et al. \(2012\)](#). For SPT-S J020258-6121.2, SPT-S J045859-5805.1, SPT-S J045912-5942.4 and SPT-S J204823-5520.7 we obtain IR luminosities and magnification factors from [Spilker et al. \(2020\)](#). For SPT-S J231124-5450.5 we use the magnification factor from [Spilker et al. \(2016\)](#). For SPT-S J235149-5722.2 we use the IR luminosity from [Faisst et al. \(2017\)](#) as an upper limit. Finally, we discard the galaxies without coordinates information in SIMBAD.

[Rizzo et al. \(2020\)](#): We adopt the values that take into account the magnification of 32.3.

[Mitsuhashi et al. \(2021\)](#): We adopt the values that take into account the magnification. These galaxies are not yet included in SIMBAD.

[Fujimoto et al. \(2021\)](#): We adopt the values that take into account the magnification (their Tables 3 and 4). These galaxies are not yet included in SIMBAD.

[Rizzo et al. \(2021\)](#): We adopt the values that take into account the magnification. For five galaxies (SPT-S J011308-4617.7, SPT-S J034510-4725.7, SPT-S J044143-4605.5, SPT-S J213244-5803.1 and SPT-S J214654-5507.9), we adopt the magnification factors from [Cunningham et al. \(2020\)](#).

Appendix B: Dataset of estimated emission line luminosities

Predictions of the eight emission lines discussed in this work (Table 1) are available at the CDS and in a Zenodo repository at <https://doi.org/10.5281/zenodo.6576202>. The dataset contains the total line luminosities as well as the contributions of the different ISM phases. We show ten rows from the dataset containing these luminosities in Table B.1 as an example of the format and content. We also present a table of the physical parameters involved in the predicted line luminosities. We show ten rows from the dataset containing the physical parameters in Table B.2 as an example of the format and content. The first column of these tables matches the Group Number in the EAGLE database ([McAlpine et al. 2016](#)), which is the unique identifier of the FoF (Friends-of-Friends) halo of a given galaxy (unique per snapshot). Although we have applied our physical model on the sample of 8 227 galaxies simulated with EAGLE, the dataset contains 8 224 galaxies since one of the galaxies does not have enough gas for the estimates, and the other two galaxies fail to predict luminosities in a reasonable amount of computational time.

Appendix C: Linear regressions for lines

Assuming that FIR luminosities change with SFR and redshift (z), we fit the estimated data to obtain linear relations in terms of these parameters for each FIR emission line. At any z there is a linear relation of the form

$$\log(L_{\text{line}}) = c_0 + c_1 \log(\text{SFR}) + c_2 \log(1+z) + c_3 \log(\text{SFR}) \log(1+z), \quad (\text{C.1})$$

with SFR in units of $M_{\odot} \text{ yr}^{-1}$ and line luminosities in L_{\odot} . The values for the coefficients presented in Table C.1 are obtained from the combination of RECAL-L0025N0752 and REF-L100N1504 mock data. We also estimate the coefficients of the [O III] and [N III] line relations using only galaxies where H II regions are dominant (the contribution is higher than 50%).

Table B.1. Example of dataset with the line luminosity estimates derived from this work.

Group Number	Sim.	z	$L_{\text{NII}57}$ dex(L_{\odot})	$L_{\text{NII}57,\text{DIG}}$ dex(L_{\odot})	$L_{\text{NII}57,\text{HII}}$ dex(L_{\odot})	$L_{\text{NII}57,\text{ato}}$ dex(L_{\odot})	$L_{\text{NII}57,\text{mol}}$ dex(L_{\odot})	$L_{\text{OII}88}$ dex(L_{\odot})	$L_{\text{OII}88,\text{DIG}}$ dex(L_{\odot})	$L_{\text{OII}88,\text{HII}}$ dex(L_{\odot})	$L_{\text{OII}88,\text{ato}}$ dex(L_{\odot})	$L_{\text{OII}88,\text{mol}}$ dex(L_{\odot})
688	Recal	0	2.93	2.93	-4.93	3.51	3.51
11	Recal	1	6.33	5.52	6.26	-0.42	-3.19	6.89	6.17	6.80	0.06	-3.56
1	Recal	5	6.48	4.55	6.48	0.60	...	7.20	5.23	7.20	1.06	...
2442	Ref100	0	6.44	4.21	6.44	-0.67	-3.13	6.90	4.83	6.89	-0.22	-3.35
4634	Ref100	1	5.30	4.97	5.03	-0.34	-2.56	5.90	5.60	5.59	0.18	-2.86
6207	Ref100	2	6.40	4.82	6.38	0.70	-4.07	7.10	5.46	7.09	1.26	-4.07
5662	Ref100	3	6.69	4.49	6.69	0.39	-4.41	7.39	5.17	7.39	0.96	-4.70
4194	Ref100	4	6.41	4.18	6.40	0.33	...	7.08	4.91	7.08	0.85	...
229	Ref100	4	5.93	5.83	5.26	1.18	-2.95	6.55	6.50	5.60	1.75	-3.31
332	Ref100	5	6.61	4.14	6.60	0.85	...	7.28	4.86	7.28	1.37	-4.70

Table B.2. Example of physical parameters dataset derived from this work.

Group Number	Sim.	z	M_{*} dex(M_{\odot})	M_{gas} dex(M_{\odot})	M_{neutral} dex(M_{\odot})	Age* dex(Gyr)	$\log(Q)$ dex(1 / s)	ISRF Habing	SFR dex(M_{\odot} / yr)	Z/Z_{\odot}	Pressure dex(K / cm ³)	$n(\text{H})_{\text{cloud}}$ dex(1 / cm ³)
688	Recal	0	8.154	7.208	6.930	0.852	34.769	0.530	-2.511	0.356	4.151	0.594
11	Recal	1	10.186	9.665	9.273	0.260	35.761	0.804	-0.409	-0.344	7.816	0.854
1	Recal	5	8.732	10.103	9.947	-0.656	44.669	1.496	0.269	-1.586	8.777	1.473
2442	Ref100	0	9.847	9.735	9.625	0.784	38.941	0.687	-0.319	-0.073	5.975	0.406
4634	Ref100	1	9.458	9.625	9.271	0.296	40.203	2.253	0.123	-0.127	7.756	1.979
6207	Ref100	2	9.151	9.846	9.410	-0.098	41.948	1.828	0.087	-0.562	7.196	1.361
5662	Ref100	3	9.057	9.854	9.566	-0.161	42.137	1.925	0.271	-0.757	7.534	1.560
4194	Ref100	4	8.682	9.814	9.449	-0.430	44.019	1.898	0.064	-1.385	7.391	1.472
229	Ref100	4	10.371	10.088	9.754	-0.346	40.174	1.466	-0.067	-1.629	7.803	1.348
332	Ref100	5	8.735	10.115	9.926	-0.690	45.148	1.757	0.420	-1.413	7.981	1.563

Table C.1. Linear relations derived from this work for each of the FIR emission lines using Eq. C.1

$\log(L_{\text{line}})$	Coefficients				1σ
	c_0	c_1	c_2	c_3	
[O III] 52 μm	6.72 ± 0.02	1.54 ± 0.02	-0.15 ± 0.03	-0.41 ± 0.03	0.63
[N III] 57 μm	6.38 ± 0.02	1.54 ± 0.02	-0.39 ± 0.03	-0.35 ± 0.03	0.61
[O I] 63 μm	6.13 ± 0.01	1.03 ± 0.01	0.70 ± 0.02	0.09 ± 0.02	0.38
[O III] 88 μm	6.84 ± 0.02	1.46 ± 0.02	-0.07 ± 0.03	-0.35 ± 0.03	0.60
[N II] 122 μm	5.59 ± 0.01	1.13 ± 0.01	-0.68 ± 0.02	0.06 ± 0.02	0.46
[O I] 145 μm	4.96 ± 0.01	1.10 ± 0.01	0.69 ± 0.02	-0.15 ± 0.02	0.41
[C II] 158 μm	6.55 ± 0.01	0.72 ± 0.01	0.14 ± 0.01	0.24 ± 0.01	0.24
[N II] 205 μm	5.48 ± 0.01	0.93 ± 0.01	-0.82 ± 0.02	0.24 ± 0.02	0.42
Coefficients for H II regions					
[O III] 52 μm	6.99 ± 0.02	1.11 ± 0.02	-0.57 ± 0.03	0.25 ± 0.04	0.53
[N III] 57 μm	6.65 ± 0.02	1.15 ± 0.02	-0.82 ± 0.03	0.26 ± 0.04	0.51
[O III] 88 μm	7.11 ± 0.02	1.06 ± 0.02	-0.48 ± 0.03	0.26 ± 0.04	0.50

Table A.1. References and number of measurements per line with a redshift range for the observational sample, after AGN dominated galaxies have been removed.

Reference	Line measurements								Redshift	
	[O III]	[N III]	[O I]	[O III]	[N II]	[O I]	[C II]	[N II]	Min.	Max.
	52 μm	57 μm	63 μm	88 μm	122 μm	145 μm	158 μm	205 μm		
Braucher et al. (2008)	45	41	158	87	100	47	223	...	0.0	1.13
Stacey et al. (2010)	9	...	1.12	1.96
Valtchanov et al. (2011)	1	1	1	1	1	1	1	...	3.04	3.04
Decarli et al. (2012)	1	3.94	3.94
Coppin et al. (2012)	6	1.1	1.62
Farrah et al. (2013)	22	23	23	...	23	23	23	...	0.04	0.26
De Looze et al. (2014)	10	4	19	...	1.1	6.6
Magdis et al. (2014)	8	15	12	0.22	2.96
Brisbin et al. (2015)	7	8	...	1.41	2.0
Spinoglio et al. (2015)	8	14	26	26	23	23	26	12	0.0	0.3
Rosenberg et al. (2015)	14	25	29	...	0.0	0.04
Ferkinhoff et al. (2015)	1	1	2.81	2.81
Gullberg et al. (2015)	20	...	2.12	5.7
Capak et al. (2015)	11	...	5.15	5.69
B��thermin et al. (2016)	1	1	4.77	4.77
Cigan et al. (2016)	5	4	5	...	5	...	0.0	0.0
Zhao et al. (2016a)	196	0.0	0.06
Zhao et al. (2016b)	7	8	...	0.11	0.2
Oteo et al. (2016)	2	...	4.42	4.43
Kamenetzky et al. (2016)	214	0.0	0.25
Pavesi et al. (2016)	3	3	5.29	5.65
Uzgil et al. (2016)	1	...	2.29	2.29
Fern��ndez-Ontiveros et al. (2016)	28	50	141	115	98	81	178	186	0.0	0.44
Knudsen et al. (2016)	1	...	6.03	6.03
Wardlow et al. (2017)	8	4	5	1.03	3.27
D��az-Santos et al. (2017)	226	148	71	...	229	...	0.0	0.09
Olsen et al. (2017)	34	...	5.15	7.6
Decarli et al. (2017)	4	...	6.07	6.59
Lagache et al. (2018)	55	...	4.22	7.91
Vishwas et al. (2018)	1	3.13	3.13
Gullberg et al. (2018)	3	...	4.42	4.44
Herrera-Camus et al. (2018a)	...	47	55	46	56	50	56	...	0.0	0.13
Lamarche et al. (2018)	1	1	1	1	1	...	2	...	1.78	1.78
Walter et al. (2018)	1	1	...	6.08	6.08
Rigopoulou et al. (2018)	1	1	1	1	1	1	1	...	2.96	2.96
Zhang et al. (2018)	9	...	25	35	38	35	33	13	1.03	3.63
Zanella et al. (2018)	9	...	1.73	1.94
Cormier et al. (2019)	...	3	30	36	15	12	41	3	0.0	0.04
De Breuck et al. (2019)	1	1	1	1	1	4.22	4.22
Tadaki et al. (2019)	1	1	1	4.34	4.34
Neeleman et al. (2019)	7	...	6.03	6.59
Lee et al. (2019)	1	...	1	1	4.69	4.69
Harrington et al. (2019)	1	2.55	2.55
B��thermin et al. (2020)	117	...	4.41	5.87
Rybak et al. (2020)	1	6.03	6.03
Harikane et al. (2020)	1	1	...	1	...	6.03	6.03
Cheng et al. (2020)	1	1	4.24	4.24
Cunningham et al. (2020)	27	37	3.07	5.81
Neeleman et al. (2020)	1	...	4.26	4.26
Rizzo et al. (2020)	1	...	4.22	4.22
Fraternali et al. (2021)	2	...	4.54	4.57
Mitsuhashi et al. (2021)	5	...	4.62	4.64
Rybak et al. (2021)	1	...	1.84	1.84
Fujimoto et al. (2021)	2	...	6.07	6.07
Lee et al. (2021)	1	4.7	4.7
Rizzo et al. (2021)	5	...	4.23	4.77